Multiwalled Carbon Nanotube Biohybrid Based Wearable Sensor

by

Irfani Rahmi Ausri

A thesis

presented to the University of Waterloo

in fulfillment of the

thesis requirement for the degree of

Doctor of Philosophy

in

Chemistry (Nanotechnology)

Waterloo, Ontario, Canada, 2022

Examining Committee Membership

The following served on the Examining Committee for this thesis. The decision of the Examining Committee is by majority vote.

External Examiner	Jie Chen Professor
Supervisor	Shirley Tang Professor
Internal Member	Juewen Liu Professor
Internal Member	Janusz Pawliszyn Professor
Internal Member	John Honek Professor
Internal-external Member	Mahla Poudineh Professor

Author's Declaration

I hereby declare that I am the sole author of this thesis. This is a true copy of the thesis, including any required final revisions, as accepted by my examiners.

I understand that my thesis may be made electronically available to the public.

Abstract

Continuous real-time surveillance of biological markers can have significant implications on disease prognosis. To date, most commercially available continuous monitoring health systems are physical sensors due to the ease of use and non-invasive detection systems. On the other hand, continuous glucose monitoring (CGM) systems that tracks ISF glucose levels are the only commercially available wearable biochemical sensors. These wearable CGM systems significantly improve patients' diabetes management and prognosis, illustrating that biochemical wearable sensor to monitor other biomarkers, such as lactate, can be highly beneficial. As a product of anaerobic metabolism, blood lactate levels are often used to evaluate health conditions such as endurance capabilities, severe infection, and respiratory failure management of critically ill patients. There are major development and commercialization of blood lactate monitoring systems, but commercially available sensors are hand-held devices that require frequent extraction of blood samples. Thus, there is dire need for a wearable lactate sensor. This thesis presents and investigates the development of wearable carbon nanotube (CNT) based lactate biosensors.

A stable enzyme matrix is one of the most important components of biosensors. Covalently linking the enzyme with glutaraldehyde is a common approach but can decrease the enzyme activity. The non-covalent technique relies on using a semi-permeable membrane, such as Nafion, to stabilize the immobilized enzymes. Nafion has been widely used for enzyme immobilization for its high stability and ionic conductivity. Our results demonstrated that the non-covalent approach retained higher enzymatic activity for the glucose sensor compared to

the covalent cross-linking technique. Through electrochemical impedance spectroscopy, the 1% Nafion membrane was shown to be stable on for 24 hours.

The incorporation of carbon nanotubes in biotransducers have improved sensors' sensitivity due to their high aspect ratio and ballistic electrical conduction due to the sp^2 hybridized carbon. However, many CNT sensor designs fail to take full advantage of the CNTs' high surface area by placing the CNTs between the enzymes and electrode, squandering a significant portion of conductive surface area that can be used to transmit signals. The multiwalled carbon nanotube (MWNT) used was grown through chemical vapor deposition and had an average diameter and length of 8.28 nm and 150 µm, respectively. Unlike commercially available MWNTs that require purification in acidic solution which consequently introduced defects, the MWNT forest was pristine and preserved the electrical properties. The MWNT was coated with chitosan (CHIT) to improve solubility and integrated in the enzyme matrix to create a porous 3D CNT-enzyme matrix. Our results show that the CNT integrated enzyme matrix slightly increased in sensitivity. The fabrication of a conductive and hydrophilic matrix depends on the optimal ratio of CNT to CHIT and CNT-CHIT to LOx.

Lastly, we developed a wearable microneedle platform that consists of a hollow microneedle array, polydimethylsiloxane (PDMS) chamber, and sensor strip. The platform utilizes a pressure-driven convection technique by designing a pumping mechanism on the top of the PDMS chamber. The platform successfully extracted up to 500 µL of solution with a viscosity comparable to blood.

This study investigates the development of biochemical sensors for continuous monitoring. Our 3D CNT-enzymatic matrix offers new insights and approaches to produce stable and sensitive sensors towards the actualization of wearable biochemical sensors.

Acknowledgements

I would like to express my deepest gratitude to my supervisor, Prof. Shirley Tang, for the constant support and guidance throughout my PhD studies. I learned how to critically think about scientific problems and continue to challenge myself to become a better scientist. I am truly grateful.

I would also like to thank my committee members, Prof. Juewen Liu, Prof. Janusz Pawliszyn, and Prof. John Honek for their time, guidance, and valuable suggestions since my first seminar, comprehensive exam, committee meetings, and up to my PhD thesis defense. I would also like to thank my internal-external examiner, Prof. Mahla Poudineh, and my external examiner, Prof. Jie Chen, for reading my thesis and attending my thesis defense.

I would like to thank Chris Kleven for his constant help setting up tools around the lab, Dr. Luis Guiterrez for training and helping me with the E-beam Evaporator, Dr.Czang-Ho Lee for training me with the tools in the G2N, and Dr. Nina Heinig for helping me with SEM.

I would like to thank my labmates and friends for all the assistance, scientific discussions, chats, and laughs: Pei Li, Dr. Yun Wu, Dr. Yael Simakov, Andrew Wenger, Gillian Guo, Dr. Monika Snowdon, Dr. Inna Novodchuk, Darren Yip, Hossein Golzar, Kyle Chu, Yuxing Wang, Zhi Li, Amanda Xu, Dr. Rob Liang, and Gillian Hawes. I would also like to thank my co-op and undergraduate students who helped me with my project: Sarah, Dragos, Agosh, Michelle, and Ellie.

Lastly, I would like to thank my mom, dad, and brothers for their unconditional support. I would also like to thank my friends Connie and Sami who makes me laugh and listen to my rants.

And finally, a special thank you for my husband, Rey, who has been with me through every step of the PhD journey; pulling me up during the tough times and sharing the joy during the good times. I would not be where I am today here without them.

Table of Contents

List of Figures

List of Tables

List of Abbreviations

3D = three dimensional

AC = alternating current

AF = atrial fibrillation

AFM = atomic force microscope

Ag Np = silver nanoparticles

ATP = adenosine triphosphate

Au = gold

Au Np = gold nanoparticles

Au-FE = flexible gold electrodes

BSA = bovine serum albumin

CE = counter electrode

CGM = continuous glucose monitoring

CHIT = chitosan

CNF = carbon nanofibers

CNT-CHIT = chitosan coated carbon nanotubes

CNT-COOH = carboxy functionalized CNTs

CNTs = carbon nanotubes

-COOH = carboxylic acid

CV = cyclic voltammetry

CVD = cardiovascular diseases

CVD = chemical vapor deposition

DM = diabetes mellitus

DMF = dimethyl formamide

DPV = differential pulse voltammetry

DWNT = double-walled carbon nanotubes

EASA = electrochemically active surface area

ECG = electrocardiogram

EIS = electrochemical impedance spectroscopy

FcME = ferrocene methanol

GA = glutaraldehyde

GOx = glucose oxidase

H_2O_2 = hydrogen peroxide

HB = β-hydroxybutarate

HPLC = high-performance liquid chromatography

HR = heart rate

HRP = horse radish peroxidase

IPA = isopropyl alcohol

ISF = interstitial fluid

K_m = Michaelis constant

LOx = lactate oxidase

LRI = lower respiratory infections

mM = millimolar

MNs = microneedles

MW = molecular weight

MWNT = multi-walled carbon nanotubes

nmol = namomolar

O_2 = oxygen

PAMAM = poly(amidoamine)

PB = Prussian Blue

PBS = phosphate buffer saline

PDDA = poly(diallyldimethylammonium) chloride

PDMS = polydimethylsiloxane

PET = polyethylene terephthalate

PFSA = perfluorinated sulfonic acid

pMB = poly methylene blue

PPG = photoplethysmography

Pt Np = platinum nanoparticles

PVC = polyvinylchloride

RE = reference electrode

RI = reverse iontophoresis

SEM = scanning electron microscope

SiO = silicon oxide

SWNT = single-walled carbon nanotubes

T1 = 1 hour hydration in PBS

T24 = 24 hours hydration in PBS

TTF = tetrathiafulvalene

WE = working electrode

ZnO Nps = zinc oxide nanoparticles

µM = micromolar

Chapter 1 Introduction

1.1 Wearable Biosensor

The most prevalent and deadliest diseases, such as cardiovascular diseases (CVD), diabetes mellitus (DB), and lower respiratory infections (LRI), have caused significant impact on quality of life and economic burden. In 2019, CVD was the leading cause of death in the world with approximately 17.9 million accounting for 32% of all deaths. [1] Approximately 537 million adults suffer from DM and caused 6.7 million deaths in 2021. [2] The COVID-19 pandemic that can lead to LRI affected approximately 370 million people and caused 5.6 million deaths as of January 2022. [3] Early and real-time diagnosis can ensure the administration of timely interventions and treatments to improve the outcome. [4, 5] However, it requires sporadic testing at health care facilities that are often time-consuming, invasive, and must be conducted by trained personnel. Thus, recent advancements in personalized wearable healthcare electronics that provide continuous real-time monitoring of biomarkers can significantly improve disease prognosis and lift the burden on the healthcare system.

To date, most commercially available continuous monitoring health systems are physical sensors due to their ease of use and non-invasive detection systems. Popular wrist-worn devices such as the Apple watch, Fitbit, and Samsung Galaxy utilize photoplethysmography to measure blood volume fluctuations through light absorption for heart rate monitoring. The Apple Watch Series 5 and 6 also have electrocardiogram (ECG) measurement capabilities with comparable performance to single-lead electrocardiograms. Studies demonstrated that the watch can be used for the screening of acute coronary artery diseases and atrial fibrillation. [6, 7] Apple and

Johnson & Johnson have launched a large-scale study called the Heartline Study to determine whether ECG data collected in the single lead format in the Apple Watches is clinically viable. [8]

On the other hand, the only commercially available wearable biochemical sensors are the continuous glucose monitoring (CGM) systems that track interstitial fluid (ISF) glucose levels such as Abbott Freestyle Libre and Dexcom CGM. These electrochemical systems utilize error modelling algorithms to account for the different glucose levels between blood and ISF to ensure clinically accurate glucose measurements.[9] In large cohort study, Dexcom's CGM system was shown to reduce hypoglycemic events in type 1 diabetic patients compared to those who used the finger-stick blood monitoring systems. [10] The improved diabetes management and prognosis demonstrate how development in wearable biochemical sensors for other diseases can be highly beneficial.

1.1.1 Skin Anatomy

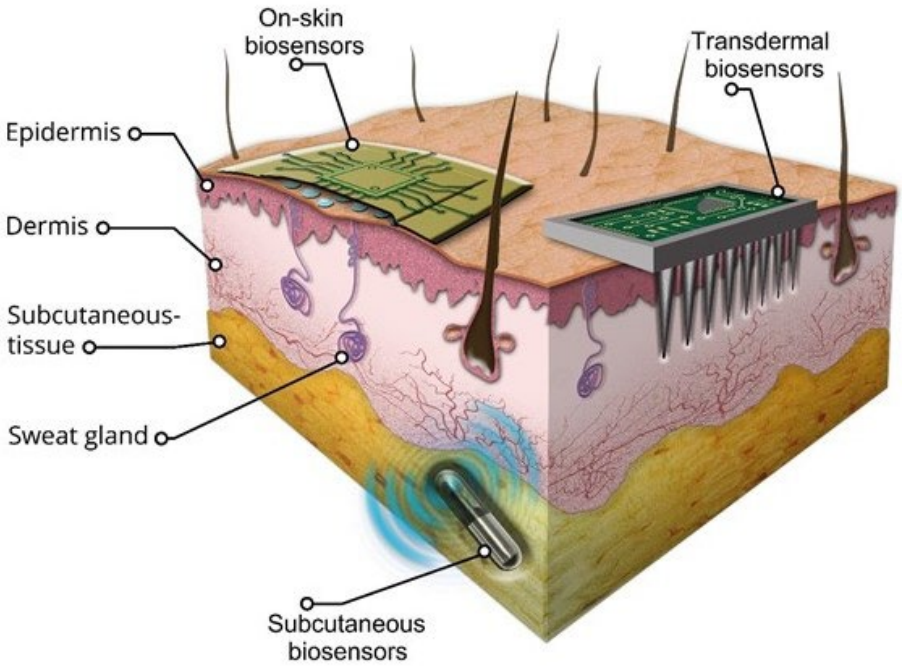

Figure 1.1 Schematic illustrating the skin's anatomy and placement of wearable sweat and microneedle sensors. [11] Reproduced with permission.

Sweat and ISF have similar biomarker composition to blood and are accessible for non-invasive and minimally-invasive monitoring through the skin. It is comprised of 3 main layers: the epidermis, dermis, and hypodermis (Fig. 1.1). The epidermis is approximately 150 µm and composed of stratified epithelium. Its outer most layer, the stratum corneum, is 10-200 µm thick and made of anucleate cells to provide hydrophobic barrier for environmental pathogens. The dermis is composed of the papillary dermis, the layer adjacent to the epidermis layer, and the reticular dermis. Its thickness ranges from 500 – 2000 µm depending on the location on the body. The last layer is the hypodermis, composed of adipocytes or fat cells, and a network of lymphatic vessels, blood vessels and collagen, also known as fibrous septa. The nerve and vascular

structures are in the deeper parts of the dermis and hypodermis. ISF fills the space outside the parenchymal cells, blood, and lymphatic vessels. [11]

1.1.2 Sweat Sensors

1.1.2.1 Physiology

Sweat plays a crucial role in maintaining skin moisture, immune defence, thermoregulation, and pH and thermoelectrolyte balance. [11] It is secreted by the secretory coils of eccrine glands upon neurotransmitter stimulation and flows to the skin through thermal ducts. [11, 12] In addition to water, ions (Na^+ and Cl^-), and metabolites, hormones, proteins, and peptides are also secreted in sweat. Sodium and chloride ions are actively transported between secretory coil and blood, creating an osmolality difference to move water into the sweat glands to produce sweat. Other than these ions, the partitioning mechanism of the other sweat components is poorly understood with some hypothesizing that the analytes passively or actively diffuse from blood or ISF and can be affected by their charge, size, and dependence on sweat rate. Some have reported that the analyte concentration ranges from mM for urea and lactate, µM for glucose, to nM or pM for proteins. [11] Their levels can further be influenced by heat, stress, chemical stimulation, or exercise. Thus, we have poor understanding of how sweat analytes reflect health status. [12] Nevertheless, the non-invasive sampling makes sweat an enticing biofluid for wearable sensor development.

1.1.2.2 Sampling

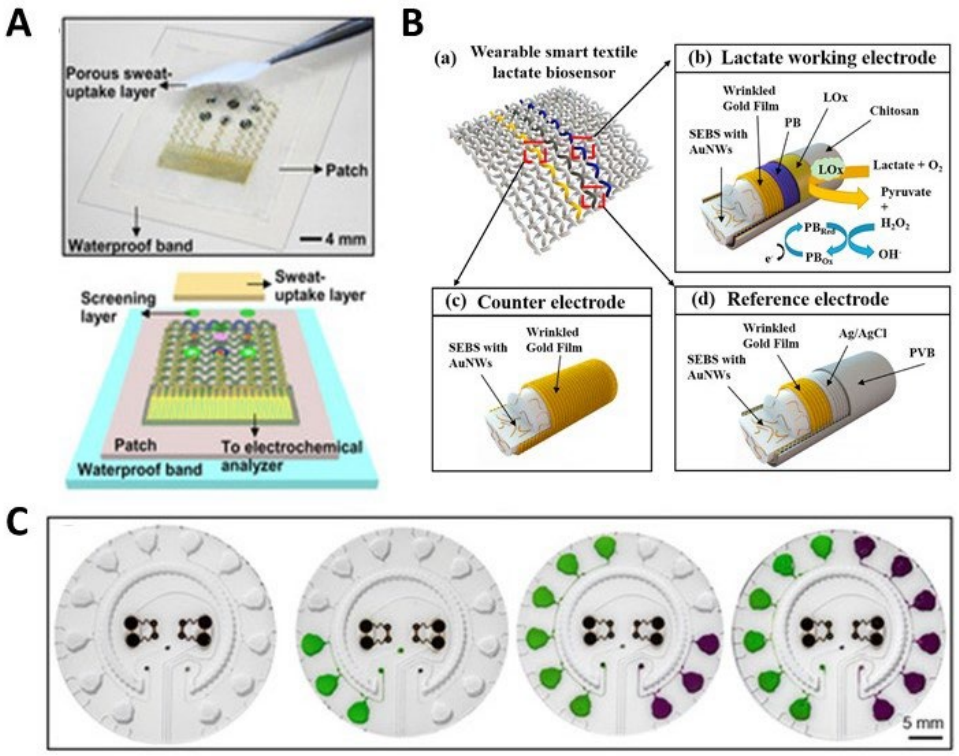

Figure 1.2 Photograph and schematics of sweat sensor designs: A) sweat patch with porous uptake layer B) textile sweat sensor C) sweat patch with microfluidic channels and microreservoirs. [13-15] Reproduced with permission.

Sweat sensors must be skin conformable and thus are often made of flexible materials such as silicone or can be integrated into fabrics (Fig. 1.2 a & b).[13, 14] During activities that generate high sweat rate, the excreted sweat is easily absorbed by the fabric or sweat uptake layer such as wood pulp-Rayon and sponge porous uptake layer (Fig. 1.2 a). [13] Microfluidic channels can also be integrated to facilitate sweat flow onto the sensor's interface. These microfluidic channels are also essential in colorimetric sweat sensors that typically contain the colorimetric reagents in microreservoirs. [15, 16] The positive pressure generated by the excreted sweat causes sweat to flow through the microfluidic channels and into the microreservoirs (Fig.

1.2 c). Bandodkar et al.'s multiplexed sweat sensor also utilized a series of microreservoirs filled with reagents to sequentially fill with sweat within 15 – 20 minutes during exercise. [15]

On the other hand, during sedentary conditions, iontophoresis, the application of a mild current between two electrodes to induce ion migration, is applied along with sweat inducing drugs such as pilocarpine to produce sweat.[17] However, prolonged use of iontophoresis can cause adverse effects such as erythema and oedema.[18] In fact, the GlucoWatch Biographer that used reverse iontophoresis was withdrawn from the market due to reports of skin-irritation. [19] Though a study reporting the integration of the programmable iontophoresis systems to personalize the applied current and density can potentially improve its safety. [20]

1.1.2.3 Wearable Sweat Sensors

Majority of the wearable sensors with on body testing were conducted with sweat sensors due to their non-invasive operation. Most were designed for glucose monitoring but alcohol, lactate, and electrolyte sensors have also been reported. One of the most advanced sweat sensors was developed by Lee et al. for diabetes management integrated with thermoresponsive microneedles containing metformin, a drug that decreases blood glucose levels. It only required 1 μL of sweat sample due to the large WE surface area composed of electrochemically deposited porous gold functionalized with Prussian Blue (PB), glucose oxidase (GOx), and Nafion. On-body experiments demonstrated that the sensor performed well compared to the commercial glucose meter Accu-Chek Performa.[13] Another enzymatic electrochemical multiplexed tattoo sweat alcohol and ISF glucose sensor also successfully monitored dynamic sweat alcohol levels with comparable accuracy to the Alcovisor Mars

Breathalyzer. [17] Transistor-based and optical sensing techniques can also be implemented for electrolyte monitoring. Lim et al.'s fiber sensor utilized PEDOT:PSS polymer for NaCl monitoring whose conductivity changes with varying concentration of NaCl. [21] Optical sensors utilize molecules that generate optical signal from colorimetric or fluorescent dyes. Bandodkar et al.'s multiplexed sweat sensor detected chloride concentration and pH levels through chemical reactions with silver chlorinate and pH sensitive dye, respectively. The silver chlorinate encased in a gel-like suspension successfully monitored chloride concentrations in sweat after exercise with good correlation to HPLC analysis.[15]

1.1.3 Interstitial Fluid and Blood Sensors

1.1.3.1 Physiology

Interstitial fluid, the fluid that surrounds parenchymal cells, as well as the blood and lymphatic vessels, constitutes 45% volume fraction of the human skin. Most of ISF is found in the dermis layer between the network of collagen and elastin fibers that limits the flow of ISF. It is formed through the extravasation of plasma from capillaries and composed of serum and cellular materials. It functions as a dynamic transport system that facilitate metabolic exchanges between cells and blood capillaries and vessels. These include transporting signaling molecules between cells, nutrients and waste between cells and capillaries, and cytokines and antigens to lymph nodes for immune regulation. [22]

Studies reported that approximately 83% of serum proteins is found in ISF at approximately 30% of the concentration in blood, likewise for serum ions. The biomarkers' concentrations are affected by the biomolecule's permeability, filtration rate, and hydrostatic

pressure through the microvasculature which can cause decreased or elevated levels in ISF compared to blood. [23, 24] For instance, ISF glucose levels generally correlate well with blood glucose at steady-state with an average lag-time of approximately 8 – 10 min but under non-steady state conditions, ISF levels can be significantly lower than blood levels. [25] ISF also contain biomarkers not found in blood such as some dermatologically relevant biomarkers. The ISF levels of tissue specific biomarkers, such as cancer biomarkers, will be approximately 1000-1500 times higher than the concentration in blood. [26] Since ISF can be monitored under sedentary conditions unlike sweat and does not clot like blood, it is an ideal surrogate biofluid for monitoring health biomarkers. [23]

1.1.3.2 Extraction

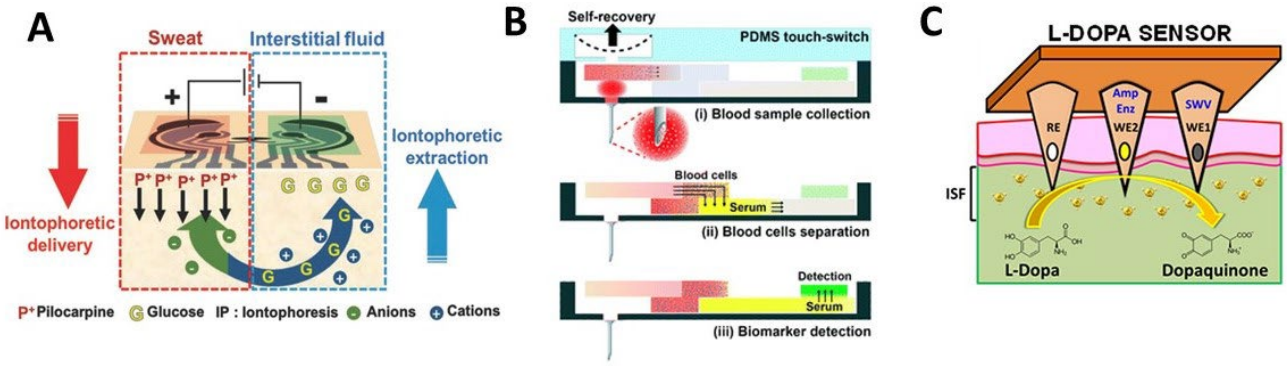

Figure 1.3 Schematic of A) iontophoretic and reverse iontophoretic sampling of sweat and ISF B) Blood/ISF extraction with a hollow microneedle sensor using a PDMS-touch switch C) ISF sampling of L-Dopa with solid microneedles fabricated by packing carbon modified paste in hollow microneedles. [17, 27, 28] Reproduced with permission.

There are two methods of ISF sampling: i) reverse iontophoresis (RI) or ii) microneedles (MNs). Non-invasive ISF monitoring is achieved through RI whereby the application of a mild current causes ions to migrate towards the cathode to facilitate the migration of neutral

biomolecules to the skin surface (Fig. 1.3 a). The glucohol sensor applied RI to extract glucose ISF but were only 1% was extracted to the skin.[17] Chen et al. improved the ISF glucose extraction onto the skin by delivering hyaluronic acid to increase the ISF osmotic pressure and prevent reabsorption.[29] MNs typically used for transdermal drug delivery for influenza or diabetes mellitus, can also be used to extract ISF (Figure 1.3 b-c). They can be 5 - 2000 µm long hollow or solid MNs made of various materials with different shapes. The MNs' length is dependent on the target biofluid and to monitor biomarkers in blood and ISF, the MNs must be >1500 µm and 100 – 800 µm in length, respectively. [30] For solid MNs sensors, the electrodes are fabricated on the MN surface to enable direct biomarkers detection in ISF. On the other hand, hollow MNs extract ISF and blood from the skin and direct it to the sensor interface in the lumen or base of the MNs. A few mechanisms of extraction have been proposed including capillary flow, osmotic pressure, and pressure-driven convention but the volume extracted were in the low µL. [31]

1.1.3.3 Wearable Microneedle Sensors

Significant advancements have been made in the development of wearable MN sensors with both hollow and solid MNs. However, due to the inherently more invasive nature of MNs, there are fewer in vivo studies compared to sweat sensors. A CGM microneedle sensor developed by Jina et al. utilized 300 µm long hollow MN array with 50 x 50 µm lumen that passively transported ISF to the sensor interface located on the opposite side of the collection chamber. The 3-electrode electrochemical system was made of GOx-bovine serum albumin (BSA) covered Pt-C working electrode (WE). When worn for 48 and 72 hours on 10 diabetic subjects, the sensor was able to monitor glucose concentration accurately compared to a commercial Free Style blood

glucose meter.[32] Hollow MN sensor systems integrated with a pressure-driven convection extraction technique have also been developed, specifically ones that employed negative pressure at the microneedle interface. Li et al. developed a paper-based multiplexed MN sensor platform that employed pumping mechanism to extract blood for cholesterol and glucose sensing. As the deformable polydimethylsiloxane (PDMS) chamber returned to its original position, sufficient pressure was generated to extract blood to the absorbent sample pad (Fig. 1.3b). The extracted blood cells were separated from serum by polysulfone membrane and transported to the reaction pads through the nitrocellulose membrane. The chamber was able to extract approximately 30 µL of blood within 10 seconds from a rabbit model and performed comparably to a reference lab-scale analyzer.[27]

Most recent in vivo continuous monitoring studies have only been tested with solid MNs, suggesting the complexity involved with hollow MNs for continuous monitoring such as biofouling induced lumen blockage. Solid MN can be fabricated by packing hollow MN with carbon paste that is either mixed with enzymes or subsequently coated with the reagent of interest. [28, 33] For example, Goud et al.'s dual-mode sensor for Parkinson management measured the oxidation of L-dopa and dopaquinone, the enzymatic product of tyrosinase (Fig. 1.3 c). It exhibited increased response with increasing levodopa concentration in both artificial interstitial fluid and skin-phantom gel. The dual-mode was designed to enhance its sensitivity due to the cross-reactivity of tyrosinase with a similar drug C-dopa. [28] Sharma et al., designed a different MNs sensor platform by using metalized polycarbonate microneedles functionalized with electropolymerized polyphenol to entrap GOx. It successfully monitored venous glucose levels

(2.6 – 20.0 mM) accurately and precisely compared to the reference YSI platform throughout a 24-hour period despite a 15-minute lag. [34]

1.1.3.4 Safety

The previously discussed MN sensors were reported to cause minimal discomfort and irritation after use. [32, 34] This is further validated by Bal et al., who demonstrated that 200, 300, 400 µm long 4 x 4 solid stainless-steel wire and 300 – 550 µm long 4 x 4 hollow MN array caused minimal discomfort and irritation that lasted less than 2 hours. They also reported that the length of MNs affected the trans epidermal water loss, as a measure of skin barrier disruption, and redness with longer MNs exacerbating the effects.[35] These studies demonstrated that MNs <1000 µm long suitable to detect biomarkers in ISF are minimally invasive. Longer MNs used to detect biomarkers in blood may cause more irritation and pain due to its penetration into deeper layers of the skin containing nerve fibers.

1.2 Lactate Physiology

1.2.1 Lactate

L-lactate is an important molecule in metabolic processes. In healthy individuals, normal blood lactate levels range between 0.3 – 1.3 mM. During aerobic metabolism, pyruvate is converted to acetyl CoA before entering Krebs cycle to produce energy. Under anaerobic conditions, pyruvate is converted to L-lactate by Lactate Dehydrogenase with NADH as a cofactor.[36] Studies have also shown that tissue, including skin, can produce lactate. Krogstad et

al., reported higher lactate levels in dermal ISF compared to venous plasma levels during fasting as measured by microdialysis catheters.[37] Erythrocytes, perivenous hepatocytes, and skeletal myocytes are also sources of lactate production. The production of lactate also releases hydrogen ions, which can be used for adenosine triphosphate (ATP) production through oxidative phosphorylation. Therefore, increased levels of hydrogen ions can occur when the oxidative is impaired and cause acidosis.[36]

1.2.2 Clinical Significance

Lactate levels can increase during any conditions that cause anaerobic metabolism, such as strenuous exercise, cardiac failure, and pressure ischemia. Hyperlactaemia or elevated lactate levels is the most relevant condition in clinical setting, which can exacerbate and cause lactate acidosis when the blood lactate is > 4mM and pH is < 7.35.[36] Blood lactate levels are often used as a biomarker to evaluate an individual's fitness level where the blood levels can increase to 12 mM and 25 mM during normal and extensive exercise, respectively.[38] When hypoxia occurs during cardiac arrest or myocardial dysfunction after cardiac surgery, anaerobic metabolism can be triggered and lead to hyperlactaemia. The increase in lactate levels is predictive of the patient's mortality.[36] It has been proposed to be used as prediction of mortality for emergency department patients with infection.[39] High lactate levels have also been observed in patients with bedsores pressure ischemia, a condition where low levels of oxygen perfuse throughout the tissue due to long-term applied force. Sweat lactate has been proposed as a biomarker for preventative measures of pressure ischemia.[40] These medical conditions demonstrate the

significance of elevated lactate levels as a predictive biomarker, highlighting the need for its monitoring in clinical settings.

1.2.3 Levels in Sweat and ISF

Studies reported conflicting results on the reliability of using sweat and ISF as blood surrogate for blood lactate monitoring. Sweat lactate levels elevate with increasing exercise intensity but only when the sweat collection method eliminates the dilution effect from increasing sweat rate. [41] However, its correlation with blood lactate levels is still disputed since sweat lactate can be generated from multiple processes such as muscle deoxygenation and thermoregulation. [41-43] The correlation between blood and ISF lactate levels is also not clear. Spehar-Délèze et al., reported that intravenous transfusion of lactate solution only raised the blood lactate levels but not in the interstitial tissue. However, the sensor detected an increase in interstitial lactate when the lactate solution was injected directly into the skin around the sensor. It was thought that the flow of lactate is hindered due to both negatively charged lactate and skin's connective tissue. Tissue dehydration could have also reduced the tissue porosity, further limiting lactate flow. [43] On the other hand, Ming et al., observed that ISF lactate levels, as measured by a microneedle sensor placed on the forearm, closely follows the increase in venous blood lactate levels during exercise. [44] These studies suggest that the source and cause of lactate production determine whether sweat or ISF can be used as a surrogate to measure blood lactate levels, which must be further investigated.

1.3 Electrochemical Biosensors

1.3.1 Electrochemistry

Electrochemistry is the branch of chemistry that studies the relationship between i) chemical changes caused by electrical energy and ii) production of electrical energy from chemical reactions. Most electrochemical sensors utilize a three-electrode system comprised of WE, counter (CE), and reference electrode (RE). When chemical reactions occur at the working electrode, the resulting current passes between the working and counter electrode. The RE controls the working electrode potential by being held at a constant potential and its composition is unaffected by the reactions that occur in the cell. Therefore, any measured changes are attributed to the working electrode. Two types of processes can occur at this electrode, faradic and non-faradic processes. Faradic processes happen when charges are transferred across the metal-solution interface and are governed by Faraday's law, whereby the flow of current measured is proportional to the amount of chemical reaction. The Nernst equation:

Equation 1-1

$$E = E^o + \frac{RT}{nF} ln \frac{C_o}{C_R}$$

Equation 1-2

$$O + ne \leftrightarrows R$$

represent the relationship between the electrode potential and concentration of the redox species where E is the electrochemical potential, E^o is the standard potential, R is the universal

gas constant, T is the temperature, F is the Faraday's constant, n is the number of electrons, and C is the concentration of the reduced or oxidized species.

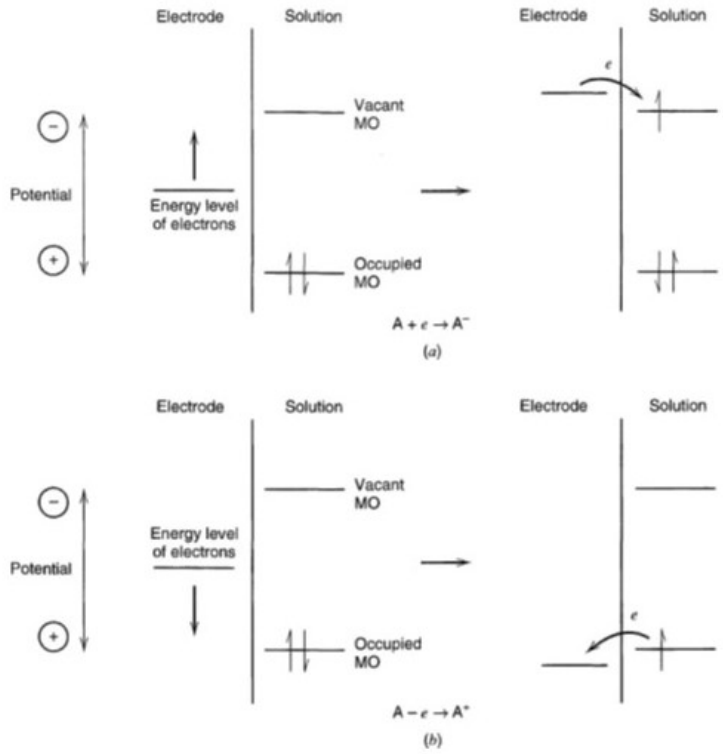

Figure 1.4 Schematic illustrating A) reduction and B) oxidation processes of molecules with the corresponding energy potentials. [45] Reproduced with permission.

This can be caused by either the oxidation or reduction of analytes (Eq. 1-2) causing electrons to flow from analyte to electrode or from electrode to analyte, respectively (Fig. 1.4). Unlike faradic processes, non-faradic processes do not involve charge transfer across the electrode. Instead, the desorption and adsorption of analytes on the electrode-solution interface upon changes in electrode potential or solution composition causes transient flow of current. [45] Understanding the behavior of electrochemical system can be achieved through multiple electrochemical

techniques such as cyclic voltammetry (CV), differential pulse voltammetry (DPV), and electrochemical impedance spectroscopy (EIS).

In biosensor, the WE detect redox molecules that correlate to the biomarker's concentration. Enzymes are often immobilized on the WE to impart selectivity but non-enzymatic strategies such as using semi-permeable membranes or artificial catalytic sites enable specific biomarker monitoring.[46, 47] There are many strategies to immobilize enzymes and they can significantly affect the sensor's performance, which will be further discussed in Chapter 2.

1.3.2 Cyclic Voltammetry and Differential Pulse Voltammetry

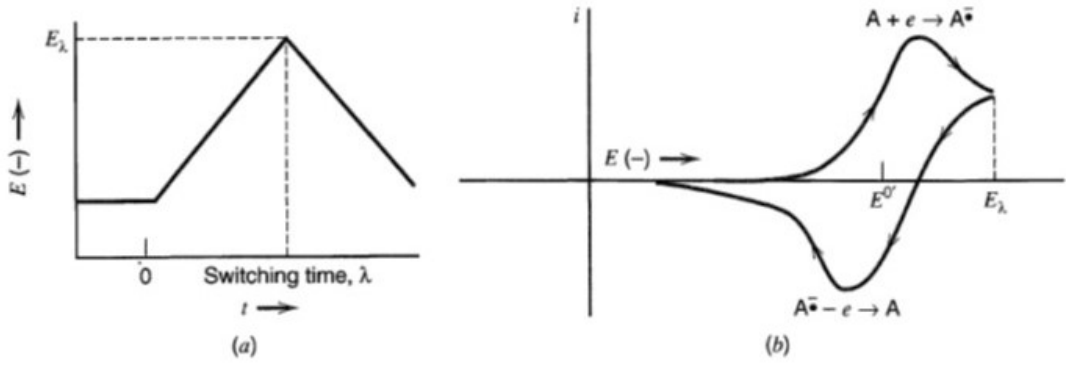

Figure 1.5 Illustrations of A) potential sweep in cyclic voltammetry B) resulting cyclic voltammogram. [45] Reproduced with permission.

CV is the most common technique used to analyze the redox processes of the electrochemical system. In this technique, a forward scan occurs when potential is swept from an initial applied potential (E_1) to a final potential (E_2). The scan is then reversed back to E_1 and the measured current demonstrate the redox processes in the system (Fig. 1.5). If the redox process is electrochemically and chemically reversible, the peak-to-peak separation should be

approximately 57 mV at 25 ^{o}C. This indicates that the analyte has a low electron transfer barrier and behaves following the Nernstian equilibrium. When the redox process has a high barrier to electron transfer, it is electrochemically irreversible and results in larger peak-to-peak separation. Furthermore, varying the scan rate of CV measurements can also determine whether the analyte is freely diffusing in solution or is adsorbed on the electrode. Increasing the scan rate decreases in the diffusion layer thickness and increases the measured current. For electrochemically reversible processes, the Randles-Sevcik equation can be used to calculate the analyte's diffusion coefficient.[48]

In DPV, background currents arising from non-Faradic processes are removed to enhance the Faradic processes. The technique starts with a baseline potential and then abruptly increased (pulsed) by 10 – 100 mV for a period of time, before dropped again to a potential higher than the previous baseline. Current is sampled right before the pulse and a few seconds after the pulse and before the potential is dropped. The difference between the two measured currents is then plotted as the DPV curve. [45]

EIS is another powerful electrochemical technique to analyze bulk properties and surface phenomena of electrical systems. In biosensors, the charge transfer resistance is used to evaluate the effects modifying the working electrodes with nanomaterials or proteins.[49] It is conducted by evaluating the effect of varying alternating current (AC) voltage frequency on the faradic impedance of an electrochemical cell. Impedance is a quotient of the voltage-time function and current-time function expressed as:

Equation 1-3

$$Z = \frac{V(t)}{I(t)}$$

It can be expressed as a modulus $|Z|$ and phase shift ($\emptyset$) in a Bode plot or as its real (Z_{Re}) and imaginary (Z_{Im}) parts in a Nyquist plot. [45] The electrical characteristics of electrochemical systems can be expressed as an equivalent circuit comprised of resistors and capacitors to represent the charge transfer resistance (R_{ct}), double layer capacitance (C_{dl}), solution resistance (R_{Ω}), and Warburg impedance (W) at a single frequency (ω). A frequently used circuit is the Randles equivalent circuit (Fig. 1.6)

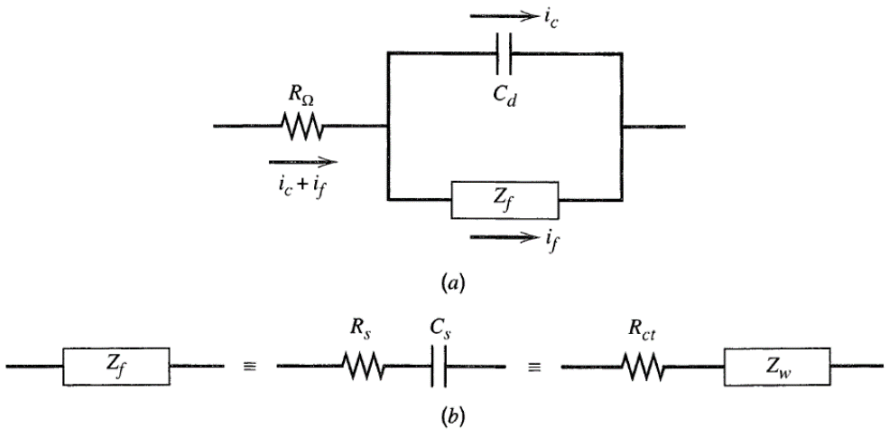

Figure 1.6 A) Randles equivalent circuit and B) Z_f represented as R_s and C_s or R_{ct} and Z_W. [45] Reproduced with permission.

The general impedance (Z) over a range of frequencies is then expressed as a combination of the real and imaginary parts:

Equation 1-4

$$Z(\omega) = Z_{Re} - jZ_{Im}$$

Equation 1-5

$$Z_{Re} = R$$

Equation 1-6

$$Z_{Im} = \frac{1}{\omega C}$$

The impedance under various applied voltage frequency can be plotted in a Nyquist plot to extract the chemical information. At low frequency, there is a linear correlation between the Z_{Re} and Z_{Im} caused by diffusion-controlled processes. At higher frequency, the R_{ct} and C_{dl} are the main processes affecting the impedance to generate a semi-circle Nyquist plot (Fig 1.7). When the electron transfer is kinetically sluggish the R_{ct} will be large creating a wide semi-circle plot, and vice versa when the electron transfer is kinetically fast. [45]

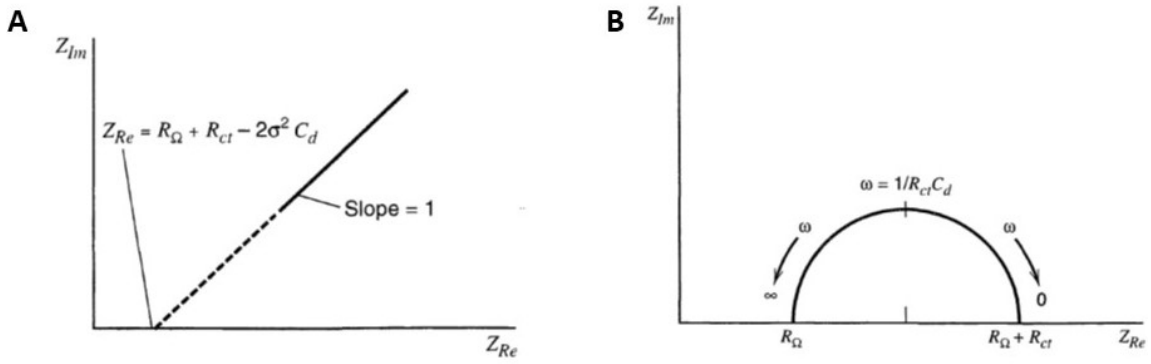

Figure 1.7 Nyquist plot at low and high frequency. [45] Reproduced with permission.

1.4 Nanomaterials

The integration of nanomaterials has consistently been shown to improve sensor performance due to increased electrochemically active surface area (EASA) and improved electrocatalytic activity. Larger EASA also increases enzyme loading to further amplify the signal. For example, Lee et al.'s nanoporous gold glucose sensor and Chen et al.'s blood glucose sensor exhibited a sensitivity of 24 and 130.4 – 196.3 μA mM^{-1} cm^{-2}, respectively, compared to Zhao et al.'s gold film sweat glucose sensor with a sensitivity of 11.7 μA mM^{-1} cm^{-2}. [13, 29, 50] Similarly, the nanoporous gold non-enzymatic sweat glucose exhibited a higher sensitivity of 253.4 μA mM^{-1} cm^{-2} compared to planar Au electrode 114 μA mM^{-1} cm^{-2}.[51, 52] Graphene, a single atom-thick nanomaterial made of carbon lattice that has excellent electrical conductivity, large surface area, and ease of functionalization, have also been used in biochemical sensors. Gold doping further increases the EASA to produce highly sensitive glucose sensor compared to bare graphene.[53]

1.4.1 Carbon Nanotubes

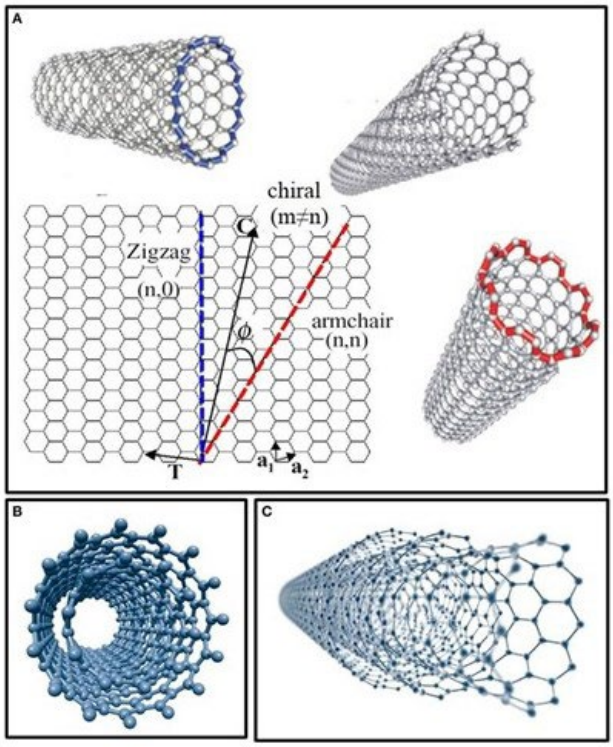

Figure 1.8 Schematics of A) single-walled CNT with different chirality, B) double walled CNT, and C) multi-walled CNT. [54] Reproduced with permission.

Carbon nanotubes (CNTs) are rolled graphene sheets that have unique properties to improve sensor performance. CNT possess superior electron transport due to its sp^2 hybridization where each carbon atom is conjugated to the adjacent carbons. [55] Consequently, they are 100 times more conductive than copper wires.[54] The sp^2 hybridization also cause them to have high thermal conductivity and mechanical/tensile strength. They are also thermally stable up to 2800^{o}C in vacuum and are chemically inert.[56]

There are different types of carbon nanotubes: single-walled (SWNT), double-walled (DWNT), and multiwalled (MWNT). Their diameters and lengths can vary depending on the

method of synthesis. Single-walled carbon nanotubes are the simplest type of CNT because they are composed of a single rolled graphene sheet with a 1 - 2 nm diameter.[57] Depending on the geometric arrangement of the carbon atoms, SWNT can be classified into three categories as illustrated in Figure 1.8, each defined by its chirality indeces (n,m). The SWNT possesses an armchair configuration when the chiral index is n = m, chiral when m 6= n, and zigzag when m = 0. Due to the one-dimensional quantum effect of SWNT, its chirality influences its conductivity such that the armchair and zig zag are metallic and semi conductor, respectively. The DWNT is composed of two layers that exist as concentric cylinders. Similar to SWNT, it has a small diameter and is able to form bundles. Lastly, the MWNT is composed of multiple cylinders of graphene sheets, have approximately 3.4 Å spacing between each layer, 2 - 100 nm in diameter, and is a metallic conductor.[57] When DWNT and MWNT are functionalized, the inner tube's mechanical and electrical properties are not significantly affected unlike functionalized SWNT.[54]

1.4.1.1 CNT Synthesis

CNTs can be synthesized using three main methods: laser vaporization, arc discharge, and chemical vapor deposition (CVD). The laser vaporization method utilizes a silica tube to produce high temperature for vaporization and a laser surrounded by argon. This method requires high-powered lasers, metal catalysts, and graphite rods with high purity. On the other hand, the arc discharge method involves the vaporization of carbon with or without a catalyst. In this method, the nanotubes in the soot are deposited on the cathodic rod after the arc discharge occurs between two graphite rods. Lastly, the CVD method is the most commonly used technique whereby thermal deposition of carbonaceous gas molecules induce the CNT formation on a

catalyst.[58] The key parameters in this method are the growth time, carbon source, temperature, and catalyst composition. This method can synthesize CNT films or forests.

1.5 Current Status of Lactate Sensors

Current commercially available blood lactate analyzers include Lactate Pro 2, Lactate Pro, Lactate Scout +, Xpress Meter, Edge, and the hand-held analyzer i-STAT. All these platforms, except for the Xpress Meter, utilized the amperometric enzymatic detection technique by analyzing the resulting electrical current produced from lactate and lactate oxidase (LOx) reaction. When compared against a standard blood laboratory analyzer, results demonstrated that no single analyzer is highly accurate over the concentration range of 1 – 23 mM. Edge and Xpress Meter are more accurate between 1 – 15 mM in clinical settings while Edge and Lactate Pro 2 are more appropriate for athletes when the blood lactate concentration ranges between 15 – 23 mM.[59] A newer device, the Lactate Pro 2, consistently measured blood lactate levels higher by a factor of 1.4 when tested on subjects rowing on the rowing ergometer.[60] Although these analyzers perform with reasonable accuracy, commercial wearable lactate sensors are not currently available.

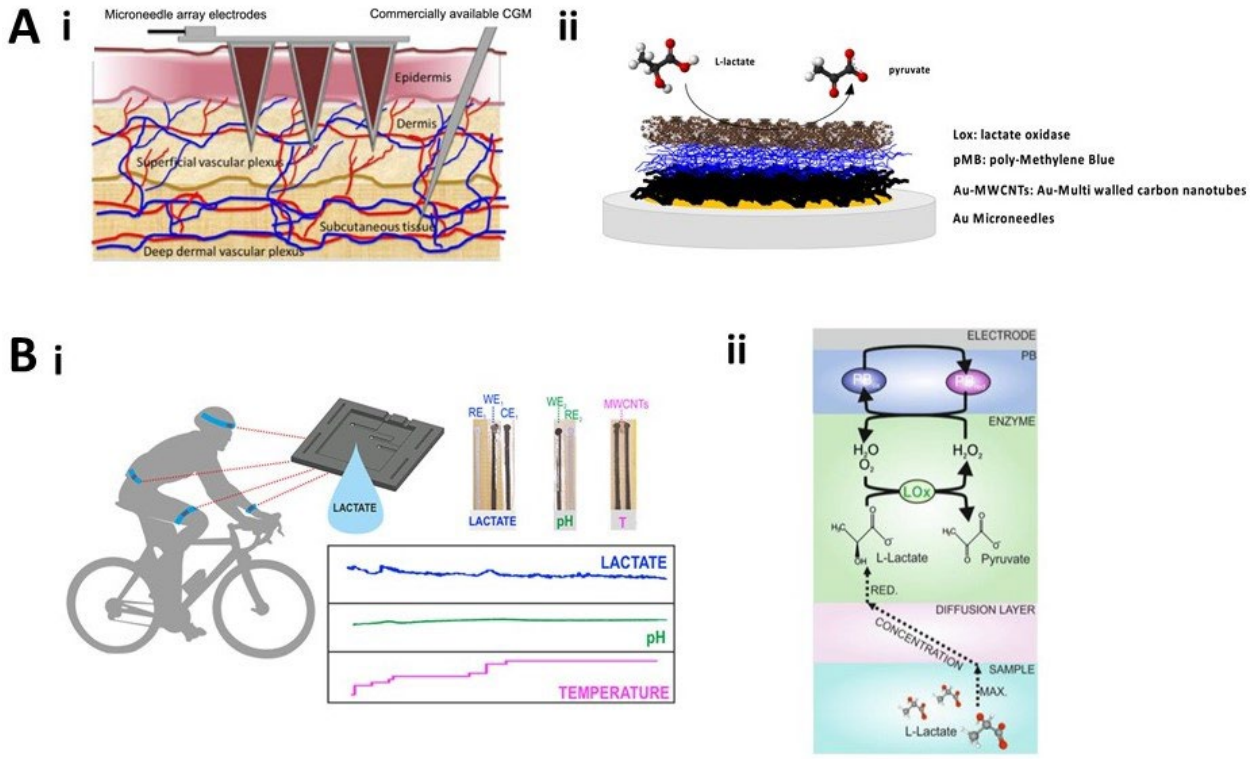

Figure 1.9 A) i. Sweat lactate sensor multiplexed with pH and temperature sensors for correctional analysis ii. Working electrode configuration and sensing mechanism B) i. Microneedle sensor for monitoring lactate ISF ii. Working electrode design. [61, 62] Reproduced with permission.

The rise of development in wearable biochemical sensors also led to progress in wearable lactate sensors. As seen in Table 1-1, sweat remains to be the most popular target for its non-invasive sampling. Contact lens sensors are an emerging category of wearable sensors and to date, there are not many lactate contact lens sensor developed. Lastly, while there are microneedle-based lactate sensors reported, they have yet to advance as fast as the sweat sensors despite their appeal as minimally invasive wearable sensor platform.

These lactate electrochemical sensors measure the redox current upon H_2O_2 reduction or oxidation, though some such as Bandodkar et al.'s multiplexed glucose, lactate, pH, chloride, and

sweat rate sensor operates similar to a biofuel cell. The enzyme catalyzed glucose/lactate oxidation and oxygen reduction produced output current proportional to the glucose/lactate concentration. This output current was converted to voltage by the resistor connecting the two electrodes. The LOx crosslinked with glutaraldehyde (GA) was immobilized on a circularly cut CNT paper functionalized with the redox mediator tetrahiafulvalene (TTF) and subsequently coated with polyvinylchloride (PVC) to prevent leaching. The sensor exhibited a linear range between 0 – 20 mM lactate and was able to detect the increasing lactate concentration during exercise. [15]

The technique of LOx immobilization can depend on the sensor format. Flexible materials are important for sweat sensors that are meant to be worn on the skin. For example, Tur-Garcia et al. sandwiched the mixture of LOx, BSA, and GA between two flexible polycarbonate membrane. The LOx, BSA, and GA mixture formed a hydrogel that easily bend with the polycarbonate membrane. [63] Wang et al. developed a textile sweat lactate sensor based on stretchable gold fiber WE coated with PB, LOx, and chitosan (CHIT). By using gold fibers, the sensor can easily be integrated into clothing and sustain stretching. The effect of stretching on the sensor must be characterized to ensure that the sensor accurately measures the lactate concentration. Under the absence of stretching, the sensor exhibited two linear dynamic range of 0 – 5 mM and 10 – 30 mM with a sensitivity of 19.1 and 2.90 $\mu A\ mM^{-1}\ cm^{-2}$, respectively. When placed under various stretching conditions, the sensor's sensitivity and current output decreased.[14] On the other hand, microneedle-based sensors are less likely to experience stretching. Therefore, the LOx enzymatic immobilization approach can aim to improve other parameters such as sensitivity. Bollella et al., fabricated ISF lactate sensor with 4 x 4 x 4 solid microneedle array functionalized with Au-MWNT, poly-Methylene Blue and LOx (Fig. 1.9 a) The

combination of both MWNT and 3-D microneedle significantly increased the EASA and improved the sensor's sensitivity to 1473 µA mM^{-1} cm^{-2} in phosphate buffer saline (PBS). As seen in Table 1-1, this sensor possessed the highest sensitivity. However, the sensitivity decreased to 178.4 and 797.4 µA mM^{-1} cm^{-2} in human serum and artificial ISF which can be attributed to the complex matrix of ISF and serum.[61]

Table 1-1 Representative Wearable Lactate Sensors

Form	Electrode Material	Linear Range (mM)	Sensitivity		Limit of Detection (µM)	K_M (mM)	Ref.
			µA mM^{-1}	µA mM^{-1} cm^{-2}			
Contact Lens	LOx-BSA-GA	0 – 1	-	53.0	-	1.75	64
Sweat Patch	Polycarbonate membrane/LOx-BSA-GA	0 - 10	0.480	-	-	5	63
Sweat Band	PB/LOx/membrane made of ETH 500, PVC, DOS	1 - 50	-6.4 x 10^{-3}	-	110	-	62
Sweat Band	SEBS AuNWs Wrinkled Au film/PB/LOx/ Chitosan	0 – 5	-	19.1	137	-	14
		10 - 30		2.90			
Microneedle	LOx/pMB/MWNT	0.01 – 0.2	-	1.47 x 10^3	2.4	0.64	61
Microneedle	LOx-BSA-GA	1 - 10	-	36.2	1.54	8.18	65

Another important parameter for biosensors is the linear range. Blood lactate levels can increase to 25 mM and sometimes higher. [38] A common technique to extend the sensor's linear range is to use a diffusion layer to delay enzyme saturation. Xuan et al., implemented this technique by fabricating a diffusion layer made of tetradodecylamonium tetrakis borate, PVC, and bis(2-ethylhexiyl) sebacate to extend the sensor's linear range from 15 – 400 µM to 1 – 50mM (Fig. 1.9 b). The diffusion layer limits the lactate flux to the LOx immobilized on PB functionalized screen-printed carbon electrodes, though at the expense of decreased sensitivity.[62]

Given the current advances in wearable lactate sensors, there is a need for further advancements in microneedle lactate sensor that continuously monitor lactate ISF. The sensor must be highly sensitive, which can be achieved by integrating nanomaterials, and have large linear range.

1.6 Motivation and Scope of Thesis

As seen in the recent advancements of wearable sensors, the monitoring of ISF as a minimally invasive surrogate biofluid to blood is more attractive than sweat due to its direct circulation with blood and comparable biomarker composition. Microneedle based sensing platforms can enable continuous ISF monitoring in real-time. Among the target biomarkers explored in the literature, wearable lactate monitoring sensors have yet to advance as much as glucose sensors even though lactate is a clinically important biomarker for many diseases such as surgical patient mortality and pressure ischemia. Furthermore, majority of the wearable microneedle sensors reported are based on solid microneedles and the performance of hollow microneedles is not well understood. Therefore, we will design a wearable lactate sensor with hollow microneedles for the continuous lactate monitoring in ISF and/or blood.

Our lab previously developed a wearable transdermal sensor consisting of an array of microneedles, a flexible three electrode electrochemical system and a crosslinked LOx bioreceptor (Table 1-1). The sensor was able to detect 1 – 10 mM lactate for up to 5 hours in buffer when placed under skin-like conditions. However, the sensor's sensitivity and specificity were lower at higher lactate concentrations and its performance decreased in blood plasma.[65]

Therefore, the overall objective of this project is to develop a highly sensitive, accurate, and stable nano-biohybrid microneedle lactate sensor. Unlike Bollella et al.'s CNT based microneedle lactate sensor, we aim to develop a conductive 3D CNT-chitosan (CNT-CHIT) enzyme matrix that can maximize the charge transfer between the enzyme and transducer (Fig. 1.10). We also aim to understand how hollow microneedles perform for continuous monitoring. The main objective is further categorized into three objectives: 1) evaluate which enzyme immobilization strategies produce a stable and sensitive sensor, 2) assess the effect of integrating 3D-CNT enzyme matrix, and 3) fabricate an on-body platform with hollow microneedles.

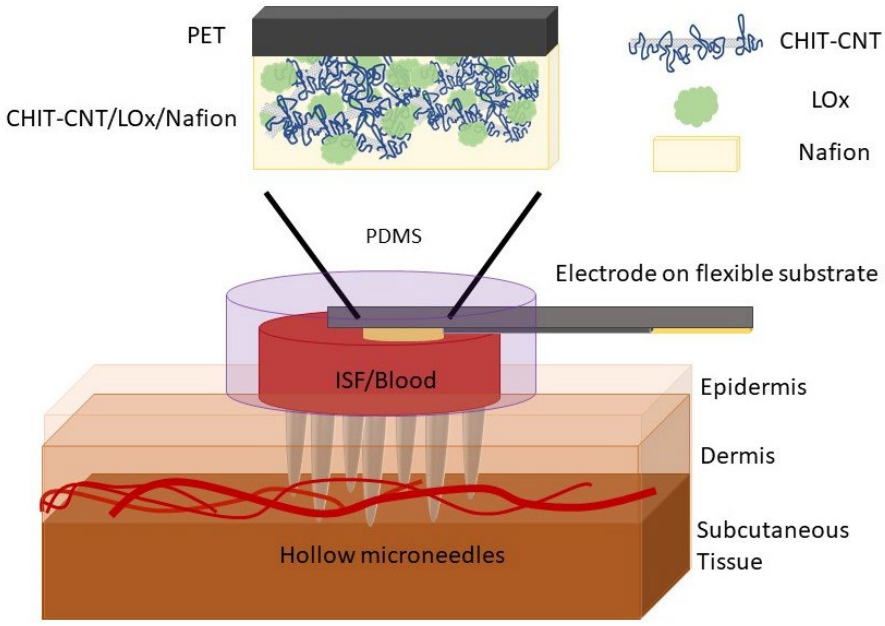

Figure 1.10 Schematic of the proposed wearable lactate sensor with hollow microneedle platform. LOx = lactate oxidase, PET = polyethylene terephthalate, PDMS = polydimethylsiloxane, ISF = interstitial fluid.

This thesis consists of 5 chapters. In **chapter 2,** I will discuss the enzyme immobilization strategy that better preserve active enzymes to produce a sensitive sensor, stability within 24 hours, and electrochemical characteristic of the enzyme matrix through DPV. We tested both covalent and non-covalent immobilization techniques. The covalent technique is similar to our

previous study and the non-covalent technique will use Nafion coating to stabilize the enzymes on the WE. Since Nafion is often reported to be permeable to positively or neutrally charged molecules, we will use glucose for the initial sensor's target biomarker. Our results show that the non-covalent approach technique produce a stable and more sensitive sensor compared to the covalent immobilization technique. The sensor's electrochemical results show that both O_2 consumption and H_2O_2 production can be used for monitoring glucose and lactate levels. In **chapter 3,** I explore the effect of integration chitosan coated MWNT into the enzyme matrix. Results show that at a 1:1 ratio of enzymes the sensor's O_2 consumption sensitivity increased after 1 hour of hydration in PBS (T1) whereas the H_2O_2 production sensitivity increase after 24 hours of hydration in PBS (T24). An increase of MWNT in the matrix at a 3:1 ratio to LOx, show decreased sensitivity in both O_2 consumption and H_2O_2 production at T1 but the increased at T24. This suggests that increased MWNT in the enzyme matrix produced a tighter and more hydrophobic matrix that require longer hydration time. In **chapter 4,** I designed a wearable PDMS-based microneedle platform using a hollow microneedle array. The platform can hold up to 500 µL of solution and the pumping mechanism can regenerate the solution. Lastly, **chapter 5** will summarize the research outcome and discuss the future of wearable sensors.

Chapter 2 Sensor Fabrication

2.1 Background

Majority of wearable sensors are electrochemical sensors due to the ease of use and miniaturization. These sensors measure the current produced from redox reaction(s) at a single or range of applied potential(s) through a three-electrode system comprised of working, counter, and reference electrodes. The WE that functions as the sensing element are often made of gold electrode functionalized with bioreceptors or non-biological molecules. Enzymes are often used as bioreceptors for their regenerability and high selectivity towards the biomarker of interest. Oxidases that use oxygen (O_2) as electron acceptors to produce hydrogen peroxide (H_2O_2) are the popular choice for developing biosensors given the redox activity of O_2 and H_2O_2. [66-68] These include GOx (Eq. 2-1), [13, 29] LOx (Eq. 2-2),[14] and alcohol oxidase (Eq. 2-3). [17]

Equation 2-1

$$D-glucose + H_2O + O_2 \xrightarrow{Glucose\ Oxidase} D-gluconic\ acid + H_2O_2$$

Equation 2-2

$$L-lactate + H_2O + O_2 \xrightarrow{L-lactate\ Oxidase} pyruvate + H_2O_2$$

Equation 2-3

$$Ethanol + H_2O + O_2 \xrightarrow{Alcohol\ Oxidase} acetaldehyde + H_2O_2$$

Other enzymes, such as dehydrogenases, that do not consume or produce redox active molecules can also be used in sensors by integrating redox mediators that reacts with the enzyme's cofactor. [69] Oxidase-based sensors operate by electrochemically monitoring the consumption of O_2 (Eq. 2-4, 2-5), as was implemented in the first GOx sensor, or production of H_2O_2 (Eq. 2-6). [70]

Equation 2-4

$$O_2 + 2\,H^+ + 2\,e \;\leftrightarrow\; H_2O_2$$

Equation 2-5

$$O_2 + 2\,H_2O + 2\,e \;\leftrightarrow\; H_2O_2 + 2\,OH^-$$

Equation 2-6

$$H_2O_2 + 2\,H^+ + 2\,e \;\leftrightarrow\; 2\,H_2O$$

Most recent wearable sensors incorporated a redox mediator PB layer that exhibits high catalytic activity towards H_2O_2 reduction.[71] These sensors indirectly detect H_2O_2 though PB reduction (Eq. 2-7, 2-8) and monitor the output current at varying biomarker concentrations at a constant applied voltage (Fig. 2.1) (-0.1 V vs. Ag/AgCl).[70, 72]

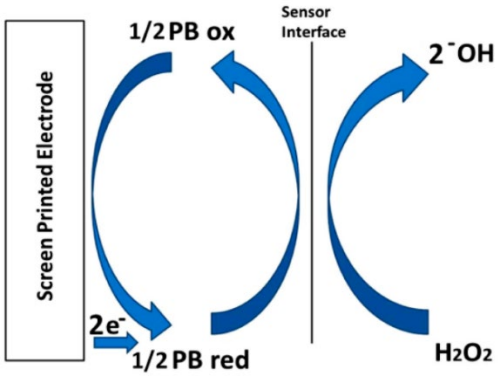

Figure 2.1 Mechanism of PB mediated H_2O_2 reduction. [73] Reproduced with permission.

Equation 2-7

$$K_4Fe_4^{II}[Fe^{\mathrm{II}}(\mathrm{CN})_6]_3 + 2\,\mathrm{H_2O_2} \;\leftrightarrow\; \mathrm{Fe_4^{III}[Fe^{II}(CN)]_6} + 4\,\mathrm{OH^-} + 4\,\mathrm{K^+}$$

Equation 2-8

$$\mathrm{H_2O_2} + 2\,\mathrm{e} \;\leftrightarrow\; 2\,\mathrm{OH^-}$$

Enzyme immobilization is the most critical part of biosensor development. The technique chosen can significantly affect the enzymes' orientation, ease of exposure to the substrate, and denaturation due to covalent or adsorption, which will impact the sensor's sensitivity, stability, and selectivity.[74]

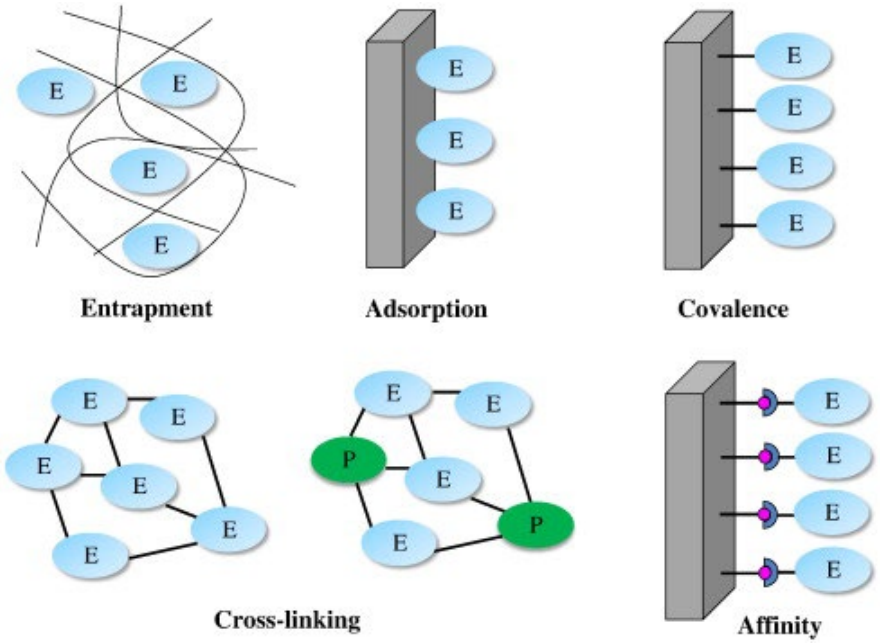

Figure 2.2 The five main strategies of enzyme immobilization on biosensors. [74] Reproduced with permission.

There are 5 main strategies of enzyme immobilization: adsorption, affinity, covalent coupling, crosslinking, and entrapment (Fig. 2.2.). Adsorption is the simplest technique where the enzyme solution is incubated on the WE for a period of time and the loosely bound enzymes are washed off. However, this approach presents the biggest stability issue since the enzymes are loosely bound and can desorb from the surface. Covalent immobilization is achieved by crosslinking the enzyme's functional groups not essential for catalytic activity onto the WE; though studies reported significant loss of enzyme activity through covalent immobilization. Affinity immobilization involves the binding between an activated group, such as avidin, on the

WE surface to a tag, such as biotin, on the enzyme. This technique aims to improve the enzymes' orientation and prevent deactivation but it requires pre-functionalization of the WE. These three strategies result in the fabrication of a thin layer enzymes that can result in low output current. Therefore, the entrapment and crosslinking strategies that enables higher enzyme loading is often preferred. Entrapment entails the encapsulation of enzymes in 3D matrices made of polymers but its stability may vary depending on the protocol. Crosslinking involves utilizing crosslinking agents, such as GA, in the presence of inert proteins to produce a protein hydrogel with some risk of enzyme inactivation.[74]

The most common strategy of enzyme immobilization is crosslinking with GA and BSA due to its simplicity. GA is a common protein crosslinking agent for its ability to react with many functional groups.[65, 72] For enzyme immobilization purposes, GA often react with the lysine residues since they are generally located on the protein surface. Though there is a potential loss in enzymatic activity due to the chemical alterations. Supporting lysine-rich inert proteins such as BSA can be used to reduce the decrease in enzymatic activity due to enzyme denaturation.[75] It is often used on sensors that are not integrated with nanomaterials to stabilize the enzymes (Table 1-1). The fabrication of the optimal crosslinked LOx matrix is dependent on the concentration of GA, crosslinking time, and BSA concentration. Since GA is the crosslinking agent, high concentration can produce tighter nanopores and potentially denature the enzyme while low concentration will not form a stable matrix. Tur-Garcia et al. showed that increasing the concentration from 5% to 10% decreased the sensitivity due to enzymatic activity loss and thus, higher enzyme concentrations was used to compensate the effect. The crosslinking time also affect the matrix formation. An increase of crosslinking time from 8 to 12 minutes increased the

sensitivity but 15 minutes crosslinking time decreased the sensitivity. [63] Thus, there is an ideal balance between stability and enzyme deactivation induced by the GA crosslinking. BSA concentration can also affect the sensor performance such that too low and too high BSA concentration may decrease the sensitivity due to the enzyme deactivation and decreased LOx-lactate catalysis, respectively. However, this parameter was not investigated in the study.

Nanomaterials often possess characteristics that enhance the enzyme immobilization through either non-covalent or covalent linkage. For example, zinc oxide nanoparticles (ZnO Nps) possess a high isoelectric point (IEP) of 9.5 while LOx has an IEP of 4.2-4.5. At neutral pH, the ZnO Nps will be positively charged while the LOx will be negatively charged, thus promoting LOx immobilization through ionic bonding. [76] Materials such as graphene with functional groups can covalently bind with the enzymes. Labroo et al., utilized the linker molecule 1-pyrenebutanoic acid succinimidyl ester to covalently immobilize LOx. [77] Additional crosslinking can be used to further ensure stability, as demonstrated by Zhu et al. who crosslinked GOx soaked in a CNT fiber with BSA and GA. [78]

Another common immobilization technique is the combination of adsorption and entrapment whereby the enzymes are dried and adsorbed on the electrode and stabilized by entrapment using membrane polymers. These membrane polymers include Nafion, chitosan, and PVC. [14, 53, 62] This technique is attractive since it eliminates the risk of enzyme deactivation due to crosslinking.

In this study we will evaluate two immobilization strategies: 1) crosslinking GOx and BSA with GA and 2) a combination of GOx adsorption and entrapment with Nafion membrane,

hereafter referred to as BSA+GA and Nafion enzyme matrix, respectively. For the second strategy, the most commonly used coating is Nafion, a type of perfluorinated sulfonic-acid (PFSA) polymer with perfluorocarbon backbone and vinylether side chains (Fig. 2.3 a).[79] Nafion films that are thicker than 25 µm are considered to be the standard membrane for polymer electrolyte fuel cells due to their efficient ion transport and mechanical stability.[80] This characteristic arises from the polymer's phase separated morphology (Fig. 2.3 b) caused by the semicrystalline polytetrafluoroethylene backbone and polysulfonyl fluoride vinyl ether (SO_3H) ionic side group (Fig. 2.3 a). [79]

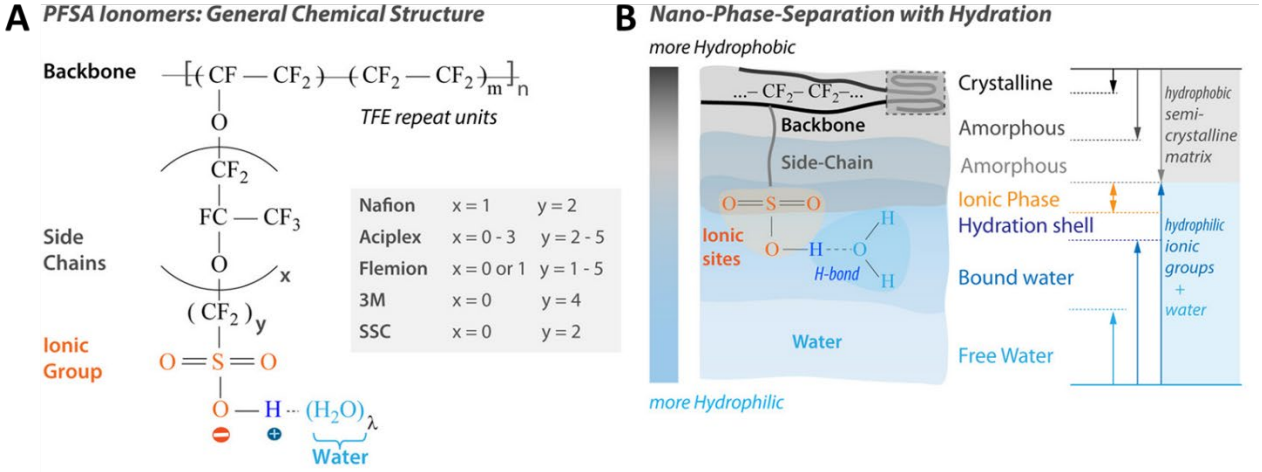

Figure 2.3 Schematic of perfluorinated sulfonic acid (PFSA): A) chemical structure and B) phase separation with hydration. [79] Reproduced with permission.

For biosensor development, the most commonly used Nafion polymers are dispersed in a mixture of approximately 20% water, 5% methanol, and 75% 1:1 1-pronanol and 2-pronanol solution. Varying concentrations from 0.5 – 5% are drop casted and dried on the enzyme layer to provide stability and reduce anti-fouling from biofluid.[13, 81] However, despite the prevalent use of thin Nafion films in biosensors, their structure and properties are not well understood.[80] The

polymer's molecular conformation in solutions is highly dependent on the solubility parameter (δ) and dielectric constant (ε) of the solvent it is dissolved in. The Nafion polymer's backbone and sulfonic acid chains possess a δ of 9.7 and 17.3 $(cal/cm^3)^{1/2}$. Solvents, such as dimethylformamide (DMF), with a similar δ to the backbone lead to low polymer aggregation with the sulfonic acid chains buried inside the coiled polymers. Methanol, ethanol, and isopropyl alcohol (IPA) have δ comparable to the polymer's sulfonic acid chain resulting in the backbone aggregation. Since methanol and IPA possess the highest and lowest δ, the backbone aggregation is more profound in methanol leading to rectangle-like structures while in ethanol and IPA the aggregates are rod-shaped. The lower ε of IPA and ethanol causes less sulfonic acid ionic dissociation and negative charge repulsion, generating more flexible polymer aggregates. Consequently, when the Nafion dispersed in alcohol are drop casted on enzyme layers, the polymers aggregation forms hydrophilic nanopores lined with sulfonic acid chains shown in Figure 2.4.[82]

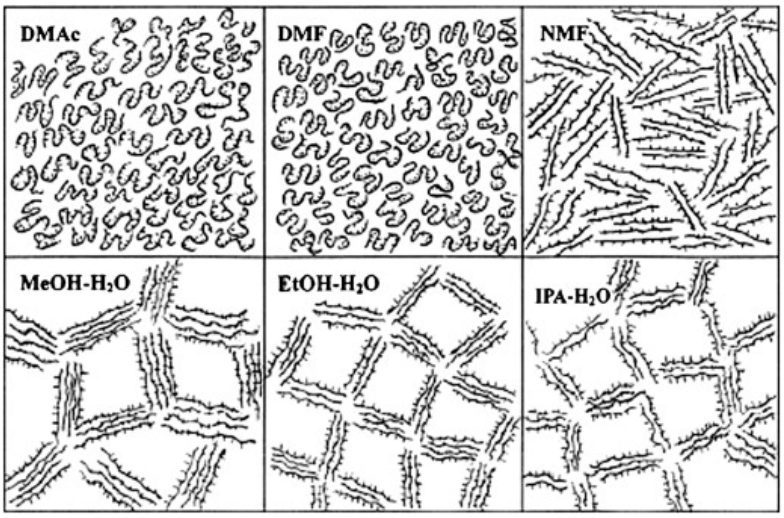

Figure 2.4 Schematic of the Nafion thin film morphology after evaporation in different solvent solutions. [82] Reproduced with permission.

In this chapter, we will present the performance of the two enzyme immobilization methods and electrochemical performance of the glucose and lactate sensors. The long-term performance of these sensors is also evaluated to determine their ability to monitor glucose and lactate over time.

2.2 Materials and Methods

2.2.1 Materials

The commercial 2 mm gold electrode, platinum microelectrode, and Ag/AgCl reference electrode were purchased from CHInsruments (Austin, Texas, USA). The polyethylene terephthalate (PET) sheets were purchased from 3M Canada. The removable vinyl sheets were purchased from Digital Graphic Inc (Mississauga, Ontario, Canada). GOx from *Aspergillus niger* (≥ 65% protein composition), 30% H_2O_2, silver nitrate ($AgNO_3$), ammonium hydroxide (NH_4OH), D-(+)-glucose (≥99.5%-GC), Sodium L-lactate (~98%), BSA (lyophilized powder, ≥ 96% - agarose gel electrophoresis), 50% GA, and Nafion 117 solution (~5% in a mixture of lower aliphatic alcohols and water) were obtained from Sigma Aldrich (Merck, Darmstadt, Germany). The recombinant LOx from *Aerococcus viridan* (≥99% purity) was purchased from AG Scientific (San Diego, California, USA). GOx and LOx possess a specific activity of 100 – 250 kU/g and 42 kU/g, respectively. Potassium ferricyanide was purchased from Avantor JT Baker (USA). Omnipur 10X PBS (DNase- and RNase-free) was purchased from Avantor VWR (USA). The potentiostat used as the CHI650A from CHInstruments (Austin, Texas, USA).

2.2.2 Flexible Gold Electrode Fabrication

The flexible gold electrodes (Au-FE) were fabricated by using a vinyl mask following the procedure developed by Wang. [83] The 3-electrodes outline was cut on the vinyl covered PET sheets using the vinyl cutter Graphtec CE7000. Excess vinyl was removed to expose the areas for electrode deposition. The Intvlac Nanochrome e-beam evaporated was used to deposit 40 nm chrome as the adhesion layer and 200 nm Au. The remaining vinyl were removed to reveal the electrodes. Insulating layer made of vinyl was designed to define the active electrode area. The solid-state reference electrode (SSRE) was fabricated following a 2-step process: 1) silver deposition and 2) silver chlorination. A vinyl mask designed to define the SSRE was placed on the sensor. A -0.5 V constant potential was applied for 8 minutes in 100 mM $AgNO_3$ in 1M NH_4OH. Excess silver was removed with milliQ water before immersed in 6% bleach for 30 seconds. After the vinyl mask was removed, nitrogen was used to dry the surface and the electrodes were left to dry overnight before use.

2.2.3 Enzyme immobilization

To fabricate the covalently linked enzyme matrix, 10 µl of 120 mg/ml GOx, 7.5 µl of 150 mg/ml BSA, and 7.5 µl of 10% GA were mixed together and drop casted on the WE. The enzyme layer was left to dry at ambient temperature and humidity for one hour. The GOx and BSA were suspended in 1x PBS at pH 7.4. The 10% GA was prepared by diluting 50% GA with MilliQ water. To fabricate the non-covalently immobilized glucose and lactate sensor, 5 µl of 60 mg/ml GOx or 6.4 µl of 50 mg/ml LOx were drop casted on the WE and dried at ambient conditions for 1 hour. Approximately 1.8 nmol of GOx was immobilized on the glucose sensor while 4 nmol of LOx was

immobilized on the lactate sensor. This was done to ensure that the amount of enzyme unit is comparable between the two sensors. A solution of 1% Nafion was drop casted on the enzyme layer and dried for 1 hour at ambient conditions. The 1% Nafion was prepared by diluting the 5% stock solution with 80% ethanol. The sensors were incubated with PBS for 1 hour prior to executing the experiments.

2.2.4 Sensor Characterization

CV, DPV, and EIS were all conducted to characterize the sensors. All of these techniques were performed using the CHI650A potentiostat. For the CV and DPV experiments, the sensor was placed in a beaker containing 1x PBS and the solution was successively spiked with concentrated 1M solution of D-glucose or L-lactate. The stir bar was turned off during CV and DPV measurements to minimize the noise. A potential range set between 0.5 - -1.0 V and scan rate of 50 mV/s were used for the CV measurements. For the O_2 and H_2O_2 DPV characterization, the same potential range was chosen but reduced to -0.1 − -0.9 V for the glucose and lactate sensing experiments. The potential increments, pulse width, sample width, and pulse period were 0.01 V, 0.1 secs, 0.01 secs, and 0.5 secs. A 10 seconds quiet time was applied prior to DPV measurements. K_3FeCN_6 dissolved in 1 mM potassium chloride (KCl) solution was used for the EIS experiments. The frequency ranged from 0.1 – $1x10^5$ Hz and the potential was held at 0 V. OriginPro 2021 Student Version from OriginLab Corporation was used to analyze and integrate the DPV plots.

2.3 Results and Discussion

2.3.1 Electrochemical Characterization

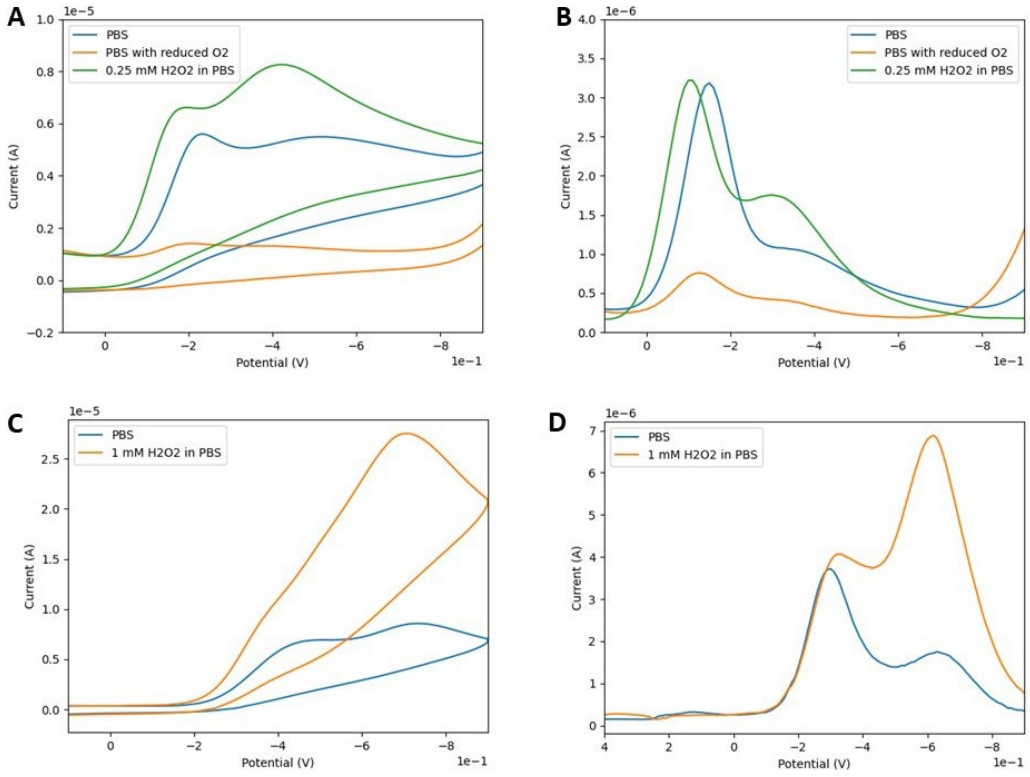

Figure 2.5 Electrochemical redox behaviour of PBS and H2O2 as measured through CV (a,c) and DPV (b,d) on: a, b. commercial gold electrodes and c, d. flexible gold electrodes (Au-FE).

Since both GOx and LOx produce H_2O_2, we first examined the electrochemical behavior of PBS and H_2O_2. Figure 2.5 a-b shows the CV and DPV of H_2O_2 in PBS on commercial gold electrodes. The peak current at approximately -0.2 V correspond to the reduction of O_2 after purging with nitrogen. The peak current at approximately -0.4 V is attributed to H_2O_2 reduction as evident by the increase in the presence of 0.25 mM H_2O_2. The H_2O_2 reduction peak is present even in the absence of H_2O_2 because O_2 reduction can produce H_2O_2 (Eq. 2-4, 2-5). These observations are consistent with Gerlache et al.'s H_2O_2 electrochemical characteristics on gold study.[84]

The dual-peak cathodic current is also observed when the PBS and H_2O_2 solutions were tested on the Au-FE (Fig. 2.5 c-d) but the peak potentials are shifted by approximately 0.2 V. Based on the Nersnt equation, the shift in potential is due to the lower Cl^- activity of the solid-state Ag/AgCl reference electrode, consistent with the report by Wang et al.[83]

2.3.2 Enzyme Immobilization

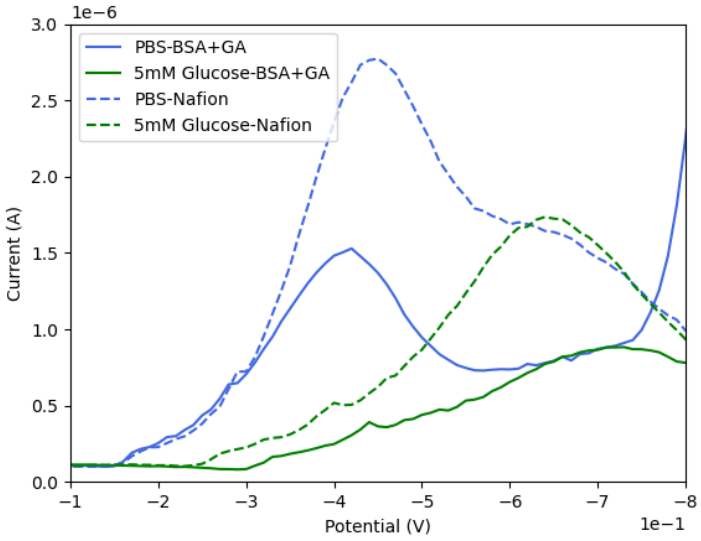

Figure 2.6 DPV of covalent (solid line) and non-covalent (stripped) glucose sensor immobilization techniques in PBS and 5 mM glucose.

We evaluated both the covalent and non-covalent immobilization techniques on glucose sensors. For the crosslinked enzyme matrix, the GOx was mixed with BSA and 10% GA. For the non-covalent approach, the GOx was dried on the WE and coated with Nafion membrane. Figure 2.6 illustrate a representative data of both immobilization techniques where both the O_2 and H_2O_2 peaks are present in PBS while the O_2 is significantly decreased in 5 mM glucose. Since O_2 is consumed upon glucose oxidation to produce H_2O_2 (Eq 2-1) the O_2 peak decreases with increasing

glucose concentrations. The Nafion matrix exhibits higher O_2 and H_2O_2 peak currents compared to the BSA+GA matrix in PBS. The O_2 peak current is a representation of the O_2 diffusing through the enzyme matrix. Therefore, the higher O_2 peak current in the Nafion matrix indicates higher O_2 permeability and availability for H_2O_2 production in 5 mM glucose. The H_2O_2 reduction peak current at 5 mM glucose is 4 times higher for the Nafion enzyme matrix than the BSA+GA matrix even though the O_2 reduction peak is 2.17 times higher. This suggests that more GOx is active to catalyze glucose in the non-covalent than the covalent immobilization technique. Although Tur-Garcia demonstrated that the enzyme matrix could be optimized, we wanted to minimize the crosslinking induced enzyme deactivation. Subsequently, the non-covalent immobilization technique was chosen to develop the wearable sensor.

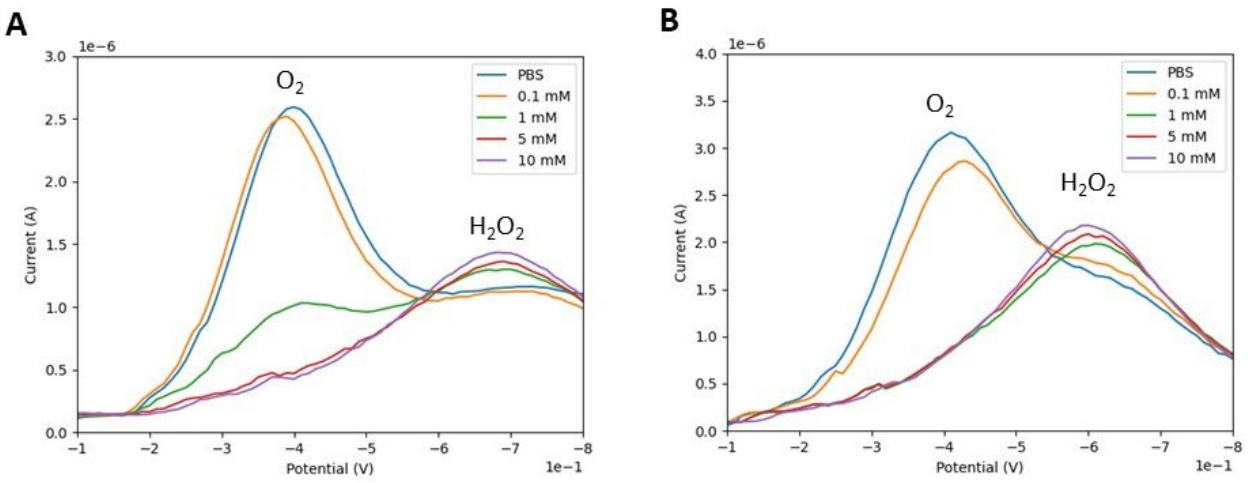

Figure 2.7 DPV of A) glucose and B) lactate sensors with increasing biomarker concentration.

Figure 2.7 a and b illustrate the successive decrease in O_2 peak current as the glucose and lactate concentration increases. On the other hand, the H_2O_2 peak current only slightly increased due to the H_2O_2 produced by O_2 reduction. The sensors show a quick response time of 2 minutes as shown by the DPV plots obtained after 100 seconds of stirring and minimal discrepancy of the

subsequent measurements. Given the dual-peak DPV curves, we evaluated the sensors' performance by analyzing the consumed O_2 and total H_2O_2 produced.[70] Since the H_2O_2 peak current does not significantly change with increasing biomarker concentration, the total H_2O_2 produced due to enzymatic catalysis is calculated by initially fitting the DPV curve as the sum of two normally distributed Gaussian curves. The total H_2O_2 is calculated by subtracting the H_2O_2 produced from O_2 reduction based on the DPV measurement in PBS.

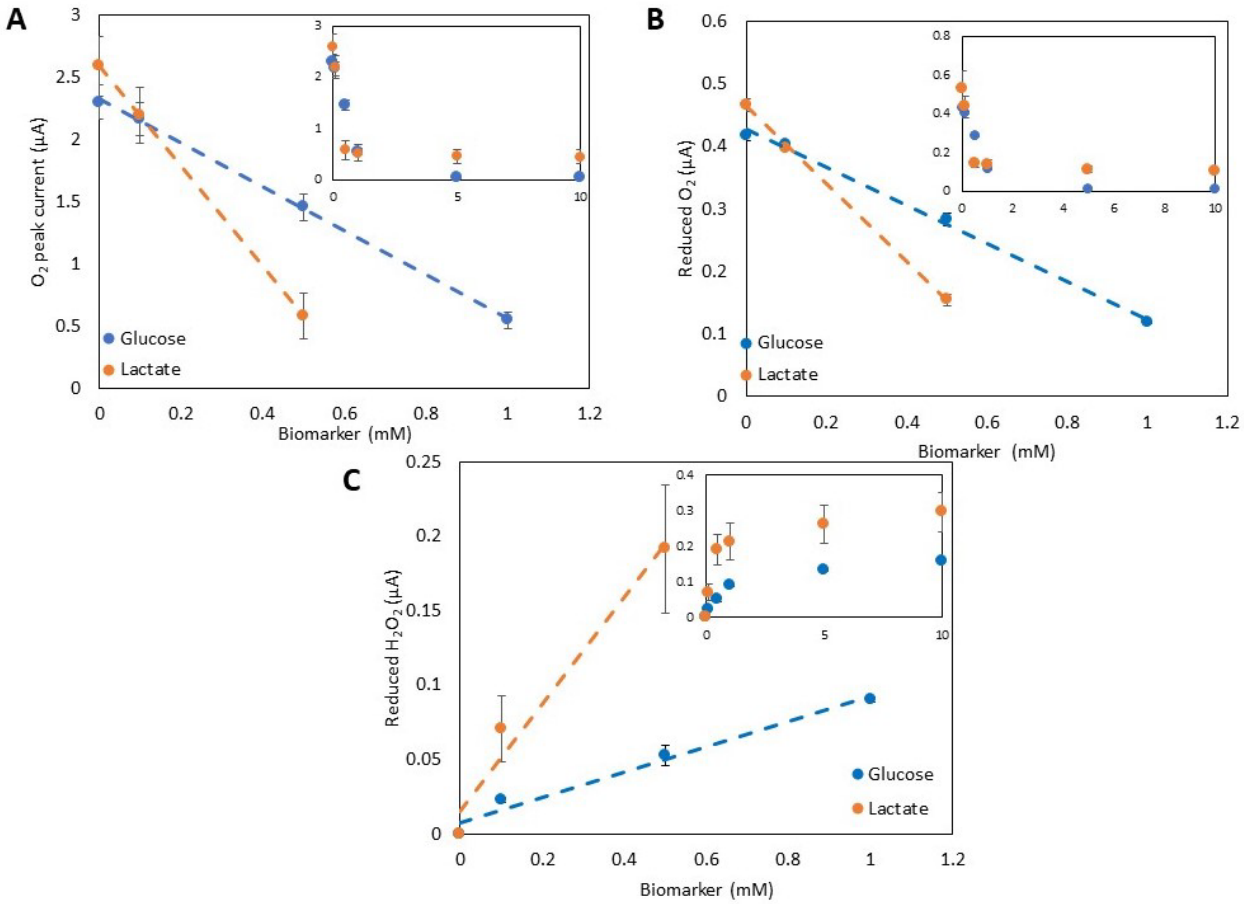

Figure 2.8 Glucose and lactate sensor calibration curve as represented by the: A) O_2 cathodic peak current, B) total O_2 reduced, and C) total H_2O_2 reduced.

In Figure 2.8 a and b, the peak current and total reduced current that are used to represent the O_2 consumption decreased as the biomarkers' concentration increased. The glucose and lactate sensors exhibited a mean saturation (V_{max}) of 5 and 1 mM and linear range between 0 – 1 and 0 – 0.5 mM, respectively. The calculated mean K_m values are 0.5 mM for the lactate sensor and at 2.5 mM for the glucose sensor. Since lower K_m values signify the enzyme's higher affinity towards its substrate, the lactate sensor shows higher sensitivity per mol of lactate ($\mu A\ mol^{-1}$) than the glucose sensor (Table 2-1).

Table 2-1 Glucose and Lactate Sensor Sensitivity

Sensor	Sensitivity ($\mu A\ mM^{-1}\ cm^{-2}$)		
	O_2 Peak Current	Reduced O_2	Reduced H_2O_2
Glucose	-29.7	-5.29	1.43
Lactate	-57.2	-10.4	4.24

The trends in K_m values are also consistent with the reported literature values of solubilized enzymes at 0.87 mM for LOx from *Aerococcus viridian* and 26 mM for GOx from *Aspergillus niger*.[85, 86] Unlike the solubilized enzymes, the K_m of immobilized enzymes are also influenced by other factors such as the enzyme's conformational changes due to immobilization techniques and biomarkers' transport kinetics. Moussa et al., reported that they observed a 3-fold decrease in K_m of the immobilized yeast D-amino acid oxidase at 1.21 mM compared to the solubilized enzymes at 3.69 mM. It was hypothesized that the observed difference was due to the enzymatic structural changes that altered the enzyme's catalytic or dissociation rate.[87] Potential build-up of products shifts the equilibrium towards the formation of EP complex (Eq. 2-9) thereby reducing the available free enzymes and decrease the K_m.[88] Therefore, all of these factors can contribute

to the immobilized enzymes' lower K_m with more profound effect on GOx than LOx. The lactate sensor's K_m values is also comparable to some of the wearable lactate sensors shown in Table 1-1 and Table 3-1.

Equation 2-9

$$E + S \overset{K_M}{\Leftrightarrow} ES \overset{K_{cat}}{\longrightarrow} EP \overset{K_p}{\Leftrightarrow} E + P$$

In Figure 2.8 c, the total detected H_2O_2 produced by enzymatic catalysis also exhibits a similar linear range as the O_2 consumption. Based on the PBS data, approximately 25% and 50% of the H_2O_2 produced from O_2 reduction is detected by the glucose and lactate sensor, respectively. The higher recovery of H_2O_2 of the lactate sensor indicates that the LOx enzyme matrix retains more H_2O_2 than the GOx enzyme matrix. Subsequently, the lactate sensor shows higher response sensitivity with at 4.24 µA mM^{-1} cm^{-2} compared to the glucose sensor at 1.43 µA mM^{-1} cm^{-2}. The lactate sensor's sensitivity is comparable to some of the wearable lactate sensors shown in Table 1-1. Although we expect varying performance between sensor strips, the O_2 consumption in both sensors shows less than 20% deviation. On the other hand, the lactate sensor exhibited larger standard deviation in the production of H_2O_2 suggesting that the matrices produced are not consistent.

2.3.3 Long Term Performance

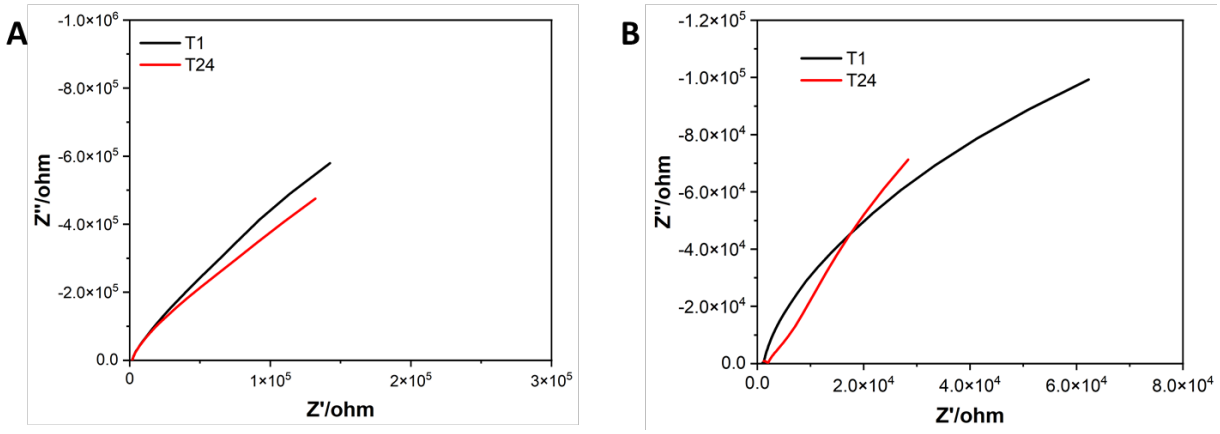

Figure 2.9 Nyquist plot of A) GOx and B) LOx sensors coated with 1% Nafion after incubated for 1-hour and 24-hours in PBS.

We employed the EIS technique to evaluate the sensor's stability to evaluate the sensors' capability for continuous monitoring. As seen in Fig. 2.9, both glucose and lactate sensors coated with 1% Nafion did not show significant impedance change after 1- and 24-hours incubation in PBS. This indicate that the Nafion created a stable membrane that coats and anchor GOx and LOx on the WE, comparable to previous studies that demonstrated stable performance for up to 24 hours. [13, 29] The Nafion coating was also applied to the counter and reference electrodes to create a continuous Nafion membrane, to further promote better adhesion to the sensor substrate.

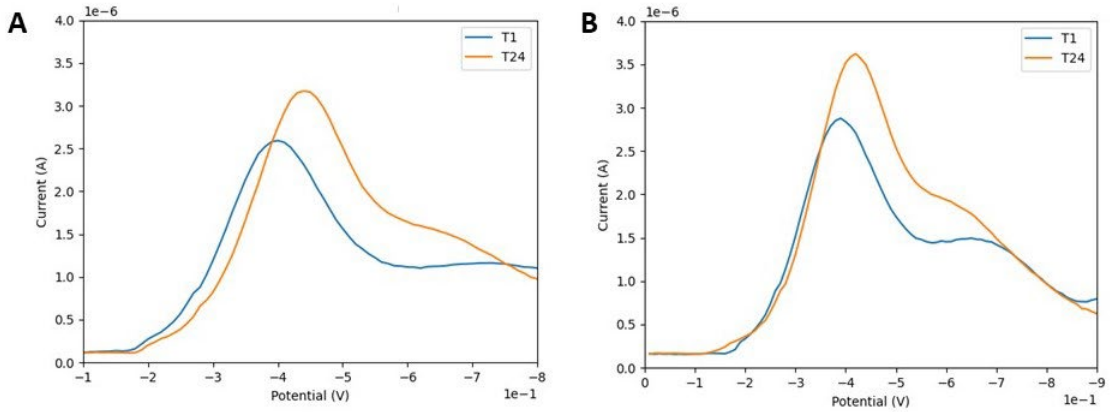

Figure 2.10 DPV graphs of PBS on A) glucose and B) lactate sensor coated with 1% Nafion at T1 and T24.

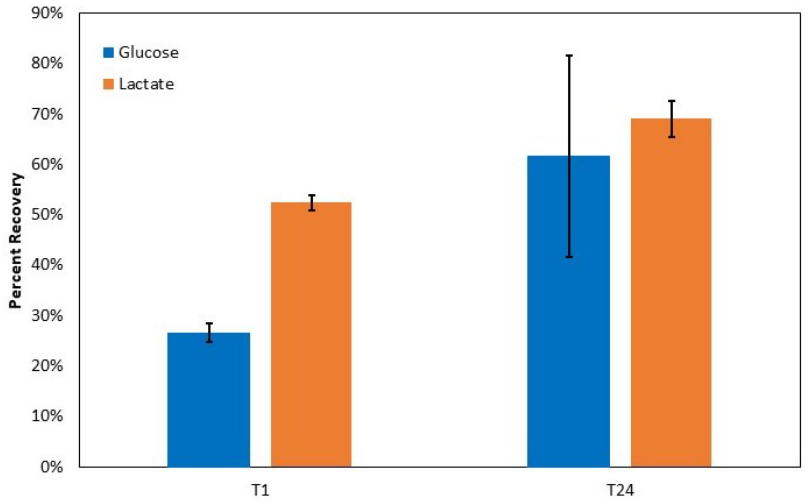

Figure 2.11 H_2O_2 percent recovery of glucose and lactate sensors after 24 hours hydration in PBS.

Furthermore, after overnight incubation in PBS at 4 ^oC, both matrices displayed higher O_2 and H_2O_2 cathodic peak current in PBS signifying higher O_2 concentration throughout the matrix (Fig 2.10) due to increased hydration. The H_2O_2 recovery improved, as shown in PBS, with the glucose sensor showing more significant increase from 27% at T1 and 62% at T24 (Fig. 2.11) but with large variation suggesting that the hydration between matrices is inconsistent.

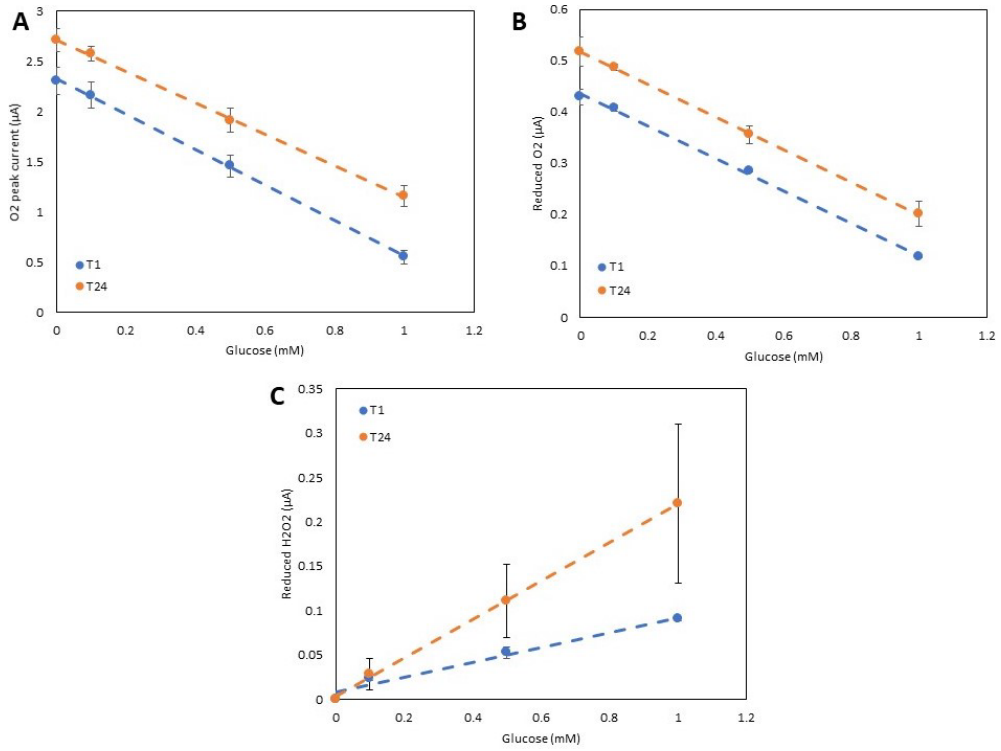

Figure 2.12 Effect of 1 and 24 hours hydration in PBS on the A,B) O_2 consumption and C) H_2O_2 production by the glucose sensor.

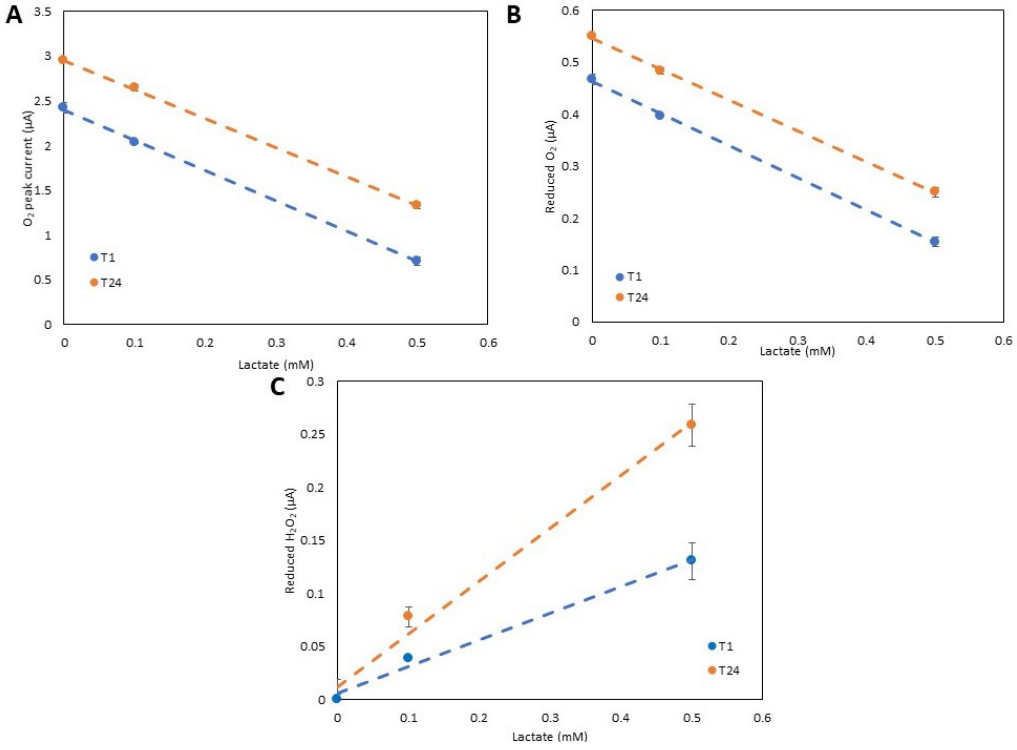

Figure 2.13 Effect of 24 hours hydration in PBS on the A,B) O_2 consumption and C) H_2O_2 production by the lactate sensor.

Matrix hydration also enabled more enzymes to actively catalyze the target biomarker. Given that enzymes have a limited shelf life, especially when they are not in their intrinsic environment, we expected the sensor's sensitivity to decrease. However, the minimal change in the sensor's sensitivity, as measured through the O_2 consumption for both glucose and lactate sensors, imply that the additional active enzymes compensated the denatured ones (Fig. 2.12 & 2.13 a-b). The sensor's sensitivity in detecting H_2O_2 produced from enzymatic catalysis (Fig. 2.12 & 2.13 c) approximately doubled from 1.43 to 3.66 and 4.24 to 8.39 $\mu A\ mM^{-1}\ cm^{-2}$ for the glucose and lactate sensors, respectively. This is due to the combined effect of increased O_2 concentration throughout the matrix, active enzymes, and H_2O_2 recovery. The glucose sensors are observed to have large sensitivity deviation in the detected H_2O_2 between sensors strips. These results demonstrate that hydration is important to ensure optimal sensor performance.

2.4 Conclusion

We demonstrated the fabrication of stable glucose and lactate sensors using the non-covalent immobilization technique on flexible substrates. Nafion formed a stable coating on the enzyme layer for 24 hours. Both O_2 consumption and H_2O_2 production from DPV measurements can be used to monitor glucose and lactate concentrations. The lactate sensor exhibits higher sensitivity than the glucose sensor, which can be attributed to the higher affinity of LOx for lactate and higher H_2O_2 recovery of the LOx matrix. Furthermore, enzyme matrix hydration enhanced the sensor's sensitivity due to increased O_2 concentration throughout the matrix, active enzymes, and H_2O_2 recovery. The linear range for the glucose and lactate sensors are 0 – 1 and 0 – 0.5 mM,

respectively. This indicates that these sensors are more suitable for detecting glucose in sweat than glucose and lactate in ISF since the blood lactate concentrations can reach up to 25 mM, beyond the sensor's operating range. As previously discussed, the sensor's K_m is affected by more than the enzyme's intrinsic affinity and enzyme saturation. The immobilization technique can restructure the enzymes and decrease their affinity towards the substrate or product build up shifting the reaction equilibrium. Some sensors reported a high linear range by using a chitosan membrane or crosslinking without BSA.[62, 72] Since enzyme saturation at µM concentrations is a common issue, some researchers implemented diffusion layers made of PVC-modified membranes to delay enzyme saturation but at the expense of reduced sensitivity. [15, 62] Furthermore, the sensor was only evaluated in buffer that is mainly composed of ions. While this sensor configuration is often reported to perform well in sweat, whose composition is more similar to buffer, ISF also contain other biomarkers that may alter the sensor output. The sensor's must be tested in ISF for at least 24 hours to also evaluate its long-term stability and performance.

Chapter 3 Carbon Nanotube Enzyme Matrix

3.1 Background

As previously mentioned, the integration of nanomaterials such as nanoporous gold, graphene, and carbon nanotubes have been proven to enhance sensor's performance. They are commonly sandwiched between the electrode and enzyme layer to increase the EASA and enhance electrocatalytic activity.[13, 15, 53] Table 3-1 lists some representative lactate sensors that are integrated with nanoparticles, graphene, and CNTs. These sensors exhibit higher sensitivity compared to the lactate sensors without nanomaterials (Table 1-1). However, the addition of silver nanoparticles (AgNp) did not exhibit a high sensitivity (0.256 $\mu A\ mM^{-1}\ cm^{-2}$) compared to ones incorporated with graphene or CNTs (Table 3-1) [89] The nanoparticles improved the sensors' performance only when the nanoparticles are deposited on graphene, carbon nanofibers (CNF), or CNTs. [76, 90, 91] In nanoparticle-graphene/CNT hybrids, the nanoparticles promote stable enzyme immobilization and electrocatalytic effect while graphene/CNT enhance the electrocatalytic effect due to their high electron transfer activity and surface area-to-volume ratio. Hashemzadeh et al., observed a significant improvement in electrocatalytic activity with successive addition of reduced graphene oxide (rGO), MWNT, and gold nanoparticles (Au Np). [91] On the other hand, Wang et al. did not observe substantial increase in electrocatalytic activity upon the addition of zinc oxide nanoparticles (ZnO Nps), suggesting that the chosen nanoparticle must be highly catalytic towards H_2O_2 to improve the sensor's performance. [76] The sensitivity and linear range of graphene and CNT integrated lactate sensors widely vary depending on additional redox mediators or proteins. The LOx/polymethylene blue (pMB)/MWNT possess the highest sensitivity and the LOx/AuNp/CNT/graphene exhibits the widest linear range. [61, 91]

Table 3-1 Representative Nanomaterial Integrated Enzymatic Lactate Sensors

Electrode Material	Linear Range (mM)	Sensitivity		Limit of Detection (μM)	K_M (mM)	Ref.
		μA mM^{-1}	μA mM^{-1} cm^{-2}			
LOx-BSA-GA/Nafion/silver nanoparticles	0 – 22	-	0.256	-	-	89
LOx/platinum nanoparticles-carbon nanofiber-poly (diallyldimethylammonium chloride) (PDDA)	0.025 – 1.5	-	36.8	11	1.6	90
LOx/gold nanoparticles/ CNT/graphene	0.05 - 100	-	35.3	2.3	-	91
LOx/1-pyrenebutanoic acid succinimidyl ester/graphene	0 – 0.02	29.9	-	0.08	0.012	77
LOx/zinc oxide nanoparticles /MWNT/PDDA	0 - 2	7.3	-	6	1.5	76
LOx-CHIT-CNT/ tetrahiafulvalene (TTF)-CNT	0 - 24	4.8	68	-	-	92
LOx/poly methylene blue (pMB)/MWNT	0.01 – 0.2	-	1.47×10^3	2.4	0.64	61
LOx/BSA/HRP/CHIT/ferrocene methanol (FcME)/MWNTs	0.0304 – 0.244	3.42	-	22.6	-	93

While the integration of CNTs improved the sensor's performance, the sandwiched configuration fails to exploit the long tubular CNT structure since majority of the enzymes are not in close proximity to the CNTs. The full potential of CNT-integrated sensors can be realized by creating a 3D CNT matrix where the enzymes are surrounded by CNTs that enabling efficient charge transfer between the enzymatic reactant or product to the electrode.

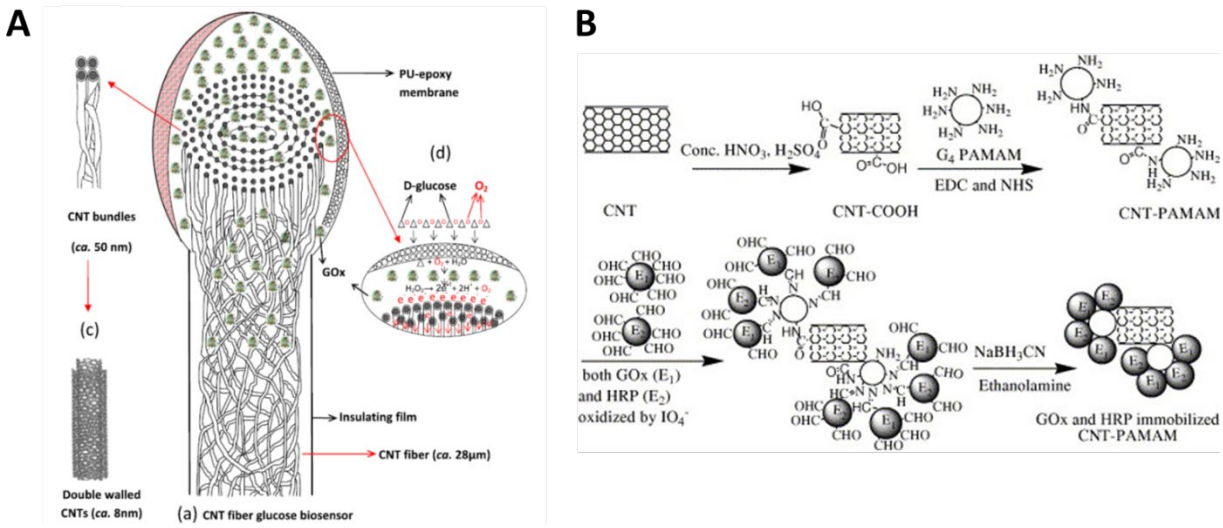

Figure 3.1 Schematics of A) CNT fiber glucose sensor and b) GOx and HRP covalently linked on PAMAM coated COOH-MWNT. [78, 94] Reproduced with permission.

Some semi-3D and 3D CNT matrices have been reported in the literature. Rernglit et al., developed a semi-3D CNT matrix by drop casting GOx solutions on dried carboxylic acid functionalized SWNTs. The GOx solution partially rehydrated the SWNT and allowed GOx to diffuse throughout the CNT matrix to produce a sensor with high sensitivity and fast response time.[95] A similar technique was used by Zhu et al. who fabricated CNT-fiber based sensors where GOx was drop casted on the CNT-fiber electrode and crosslinked with BSA and GA (Fig. 3.1 a).[78] On the other hand, 3D- CNT enzyme matrix fabrication entails the mixing of CNT suspensions and enzyme solution before drying on the electrode surface. Since CNTs are hydrophobic, suspending CNTs in aqueous solution can be achieved through either acid (HNO_3:H_2SO_4) treatment to introduce carboxylic acid (-COOH) functional groups, which also purifies the CNTs, or coating with amphiphilic polymers or enzymes. Similar to Rernglit et al.'s sensor the carboxy-functionalized CNTs (CNT-COOH) can be directly mixed with the enzymes allowing the enzymes to adsorb on the defect-free surfaces.[96] The carboxylic groups can also act as anchoring sites for the

immobilization of multiple enzymes. Zeng et al. anchored the dendritic macromolecule poly(amidoamine) (PAMAM) through EDC-NHS chemistry to act as additional immobilization sites for GOx and horseradish peroxidase (HRP) (Fig. 3.1 b). The enzymes' peripheral carbohydrate groups were oxidized to carbaldehyde with periodate for immobilization on PAMAM. The integration of CNT was vital for the HRP charge transfer, a necessary process in the glucose sensing principle.[94] Likewise, Hua et al., reported that MNWT-COOH/polyaniline composite generated a synergistic effect of strong enzyme affinity and enhanced electron transfer HRP's active site for H_2O_2 detection.[97] A unique fabrication strategy was developed by Hernandez-Ibanez et al. who created a porous chitosan biopolymer through a phase-inversion technique. An aqueous solution comprised of HRP, BSA, and LOx displaced the dimethylformamide and methanol solvents used to suspend MWNT-COOH, ferrocene methanol redox mediator, and chitosan to form the porous 3D-enzyme matrix.[93] Even though carboxy-functionalized CNTs can promote increased and stable enzyme immobilization, acid treatment compromises the electrical properties.[98]

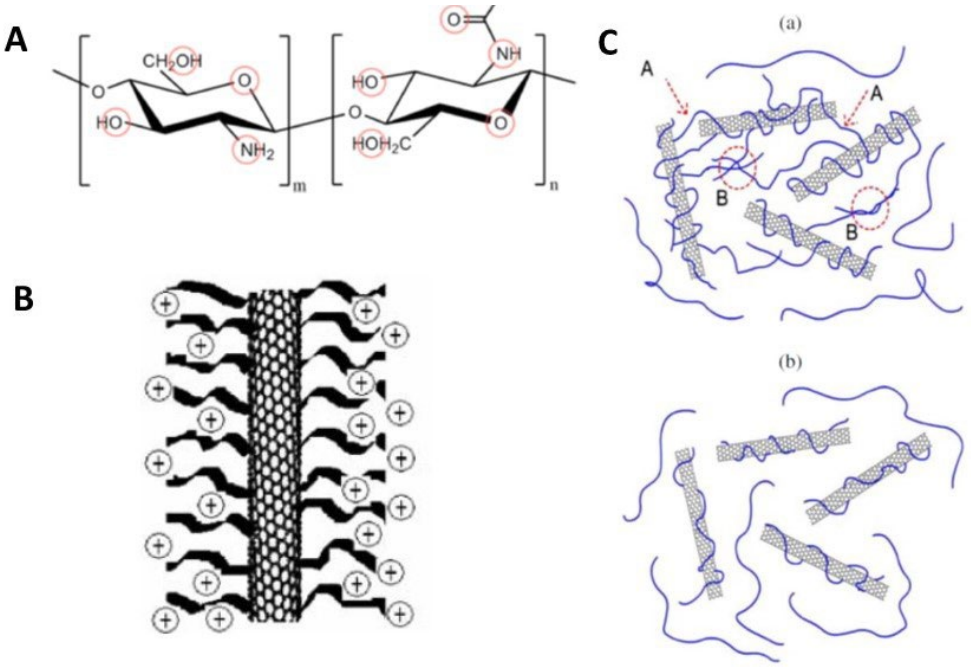

Figure 3.2 Schematics of: A) chitosan comprised of N-acetyl-D-glucosamine and D-glucosamine. The red circles indicate the functional groups that can participate in hydrogen bonds. B) chitosan-coated CNT with the protonated amine group facing away from the hydrophobic CNT surface. B) effect of high (a) and low (b) chitosan concentration with higher concentration causing entanglement between chitosan polymers. [98-100] Reproduced with permission.

Alternatively, CNTs can be coated with polymers or proteins for solubilization in aqueous solutions, with chitosan being one of the most popular choices.[98, 101-103] Chitosan is a polysaccharide biopolymer produced from the deacetylation of chitin found on shrimp or carb shells. It is comprised of N-acetyl-D-glucosamine and D-glucosamine units connected by β-1,4-linkages (Fig. 3.2 a). The degree of deacetylation is defined by the percentage of N-acetyl-D-glucosamine units, which determines its solubility in dilute acidic solutions. It is biocompatible, biodegradable, and easily modified due to the presence of carboxyl and amino groups.[99] Consequently, chitosan has a wide range of application including the development of hydrophilic membranes. [99, 104] A solution of 1% chitosan dispersed in 1 or 2% acetic acid is often used to coat

CNTs and can be used to modify the electrode surface or as a 3D-matrix.[49, 98, 103] The sensors that utilized CNT-CHIT as a 3D- enzyme matrix detected the direct electron transfer from the glucose dehydrogenase NADH co-factor or GOx redox mediator.[98, 103] Chitosan in acidic solutions adsorb and wrap around CNTs similar to cationic surfactants with the protonated amine groups facing away from the CNT (Fig. 3.2 b).[98, 100] The methyl groups of N-acetyl-D-glucosamine are likely to form hydrophobic interactions with CNT, similar to Lee et al.'s study on mica.[99] Increasing concentrations of chitosan have been shown promote CNT aggregation as hydrogen bonds are formed between wrapped- and free- chitosan (Fig. 3.2 c).[99, 100] At the neutral pH of sensing experiments, the chitosan polymers become more rigid due to the deprotonation of amine groups.[99] Therefore, the CNT-CHIT composite is an attractive choice to form a conductive hydrophilic 3D-matrix.

Payne et al., have previously reported the development of SWNT-CHIT based sensor composed of LOx-CNT-CHIT enzyme matrix and tetrathiafulvalene (TTF)-CNT redox mediator layer. The study investigated the effects of CHIT concentration, CNT percentage, and enzyme loading on the enzyme matrix. It was observed that the optimal CHIT concentration is 0.6% such that lower concentrations produced an unstable matrix while higher concentrations prevented lactate-LOx interaction. The ideal CNT-CHIT percentage loaded was 1%. At higher percentage, the CNT crowded the LOx and prevented lactate oxidase catalysis. On the other hand, a lower percentage reduced the charge transfer between CNTs. Furthermore, they observed that the optimal enzyme loading is 7.5 units per sensor. The sensor's sensitivity decreased at lower and higher loading due to chitosan induced resistive loss and matrix instability, respectively. [92] Although this study explored a similar intended CNT-matrix, there are some factors that must be

further investigated including the effect of low and high molecular weight (MW) CHIT on CNT-CHIT length and the CNT type. The CNT-CHIT length is a crucial parameter because it defines the matrix network percolation. If the CNT-CHIT length is sufficiently long, low CNT loading can produce a conductive network. The length of CNT-CHIT is also dependent on the CNT suspension with low and high MW. Higher MW CHIT can potentially coat the MWNT better than low MW CHIT, thus it will not require extensive sonication and better preserve the CNT length. Furthermore, SWNT are less rigid than MWNT and thus will generate tight nanopores that prevent the LOx-lactate interaction. [105] The rigid MWNT may form larger nanopores that can prevent this issue. Hereafter, the MWNT-CHIT will be referred to as CNT-CHIT. In this chapter we will investigate the CNT-CHIT matrix for lactate sensing

3.2 Materials and Methods

3.2.1 Materials

Silicon oxide (SiO) wafers were purchased from Silicon Valley Microelectronics (Santa Clara, California, USA). The compresses gases were obtained from Linde Canada. Tap300-G tapping mode atomic force microscopy probes were purchased from Budget Sensors (Sofia, Bulgaria). Chloroform (99%), H_2SO_4 (95.0 – 98.0 %), H_2O_2 (30 wt. % in H_2O, contains inhibitor), acetone (≥ 99.5%), isopropyl alcohol (≥ 99.9%, suitable for HPLC), (low MW CHIT (50 – 190 kDa, ≥ 75% deacetylated), acetic acid (≥ 99%), sodium L-lactate (~98%), BSA (lyophilized powder, ≥ 96% - agarose gel electrophoresis), and Nafion 117 solution (~5% in a mixture of lower aliphatic alcohols and water) were obtained from Sigma Aldrich (Merck, Darmstadt, Germany). The

recombinant LOx from *Aerococcus viridan* (≥99% purity) was purchased from AG Scientific (San Diego, California, USA). Potassium ferricyanide was purchased from Avantor JT Baker (USA). Omnipur 10X PBS (DNase- and RNase-free) was purchased from Avantor VWR (USA). The potentiostat used as the CHI650A from CHInstruments (Austin, Texas, USA). The ultrasonic bath, Elmasonic P 30 H (115V), was manufactured by Elma Ultrasonic.

3.2.2 MWNT Fabrication

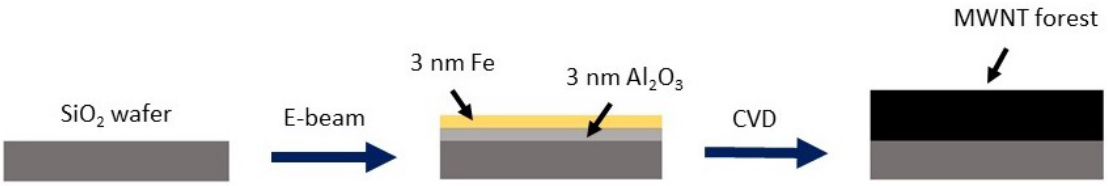

Figure 3.3 Schematic of the MWNT fabrication process: 3 nm Al2O3 and 3nm Fe are sequentially deposited with e-beam deposition before grown in CVD.

The highly aligned MWNT forest fabrication is shown as a schematic in Fig. 3.3. The 3 nm iron (Fe) and 3 nm Aluminum Oxide layers were deposited through e-beam deposition using the Intvlac thermal/E-beam evaporator. MWNT forest was grown through chemical vapor deposition at 725 ^{o}C in an Angstrom CVD with a 1" quartz tube following the protocol developed by Shadmehr et al.[106] A mixture of argon: hydrogen: ethylene gasses at 70:70:70 sccm was used as the carbon source. The growth time can be varied depending on the desired length and with a growth time of 5 minutes, the MWNT forest length grew to 150 µm.

3.2.3 MWNT Forest Characterization

The MWNT forests were characterized using the Zeiss Ultra scanning electron microscope (SEM) and Digital Instrument's Multimode atomic force microscope (AFM). The SEM images were obtained under 5 or 20 kV accelerating voltage. Gwyddion 2.60 was used to conduct sectional analysis of the AFM images. The AFM samples were prepared on SiO wafers cleaned with a 3:1 mixture of H_2SO_4:H_2O_2 piranha solution for 20 minutes then rinsed with MilliQ water, acetone, and isopropyl alcohol and dried under nitrogen. The MWNT was dispersed in chloroform at 0.1 mg/ml and sonicated in an ultrasonic water bath for at least 4 hours. The MWNT suspension is left to sit for a few hours to let the remaining aggregates to settle. The MWNT suspension is drop casted on the cleaned SiO wafer and left to dry before imaging.

3.2.4 CNT-CHIT Enzyme Matrix Fabrication

The CNT-CHIT suspension was prepared by sonicating the MWNT forest at 1 mg/ml in 1% chitosan solution dispersed in 2% acetic acid in an ultrasonic bath at 20 minutes intervals for at least 2 hours until a homogenous suspension is achieved. The ultrasonic bath was set at 80 kHz and 100% power.

To fabricate the enzyme matrices a mixture of 100 mg/ml LOx was mixed at a 1:1 ratio with PBS, 1% chitosan, or the CNT-CHIT suspension and 6.4 µl of the solution was drop casted on the WE. The enzyme matrices were left to dry at ambient conditions for 1 hour. This protocol produces the 1:1 CNT-CHIT+LOx enzyme matrix. To fabricate the 3:1 CNT-CHIT+LOx enzyme matrix, a mixture of 200 mg/ml LOx was mixed at a 1:3 ratio with the CNT-CHIT suspension. This

ensure that the amount of enzyme units remains constant for all matrices. A solution of 1% Nafion was then drop casted on the enzyme layer and dried for 1 hour at ambient conditions. The 1% Nafion was prepared by diluting the 5% stock solution with 80% ethanol. The sensors were incubated with PBS for 1 hour prior to executing the experiments.

3.2.5 Electrochemical Experimental Procedure

Similar to the protocol outlined in chapter 1, the electrochemical experiments were conducted using the potentiostat. For the CV and DPV experiments, the sensor was placed in a beaker containing 1x PBS and the appropriate solution was added in. A 1 mM K_3FeCN_6 solution dissolved in PBS was used for the CNT-CHIT characterization. A potential range set between 0.5 - -0.3 V and scan rate of 50 mV/s were used for the CV measurements. Concentrated 1M solution of L-lactate was spiked into PBS and the stir bar was turned off during DPV measurements to minimize the noise. A potential range set between -0.1 − -0.9 V for DPV measurements. The potential increments, pulse width, sample width, and pulse period were 0.01 V, 0.1 secs, 0.01 secs, and 0.5 secs. A 10 seconds quiet time was applied prior to DPV measurements. OriginPro 2021 Student Version from OriginLab Corporation was used to analyze and integrate the DPV plots.

3.3 Results and Discussion

3.3.1 Growth of Aligned MWNT Forest

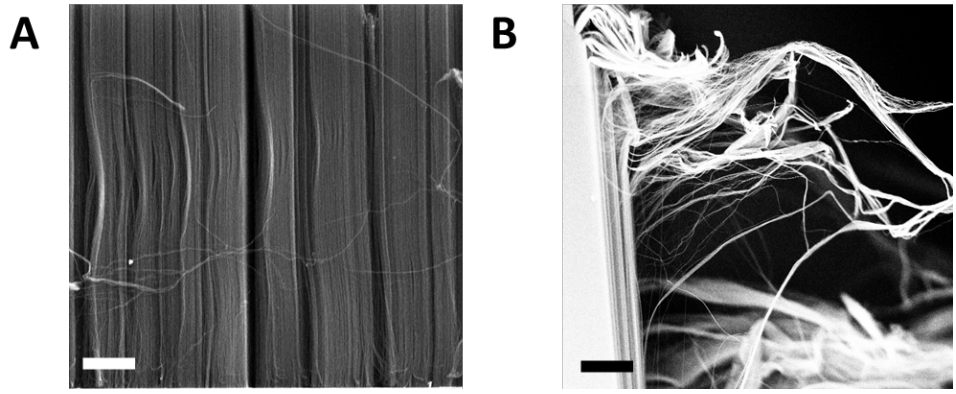

Figure 3.4 SEM images of the A) aligned and B) thread-like MWNT forest. The white scale bars correspond to A) 20 and B) 40 µm.

As seen in Fig. 3.4 a, the CVD- grown MWNT forest SEM are highly aligned due to the van der Walls interactions between the pristine hydrophobic CNT surfaces. Consequently, when edges of the CNTs are pulled, the strong van der Walls forces also pulls the neighboring CNTs to create thread-like structures (Fig. 3.4 b). The MWNT forest's length if dependent on the growth time such that a 30- and 5- minute growth produce 800 and 150 µm, respectively. These findings are consistent with other CVD-grown aligned CNT.[107]

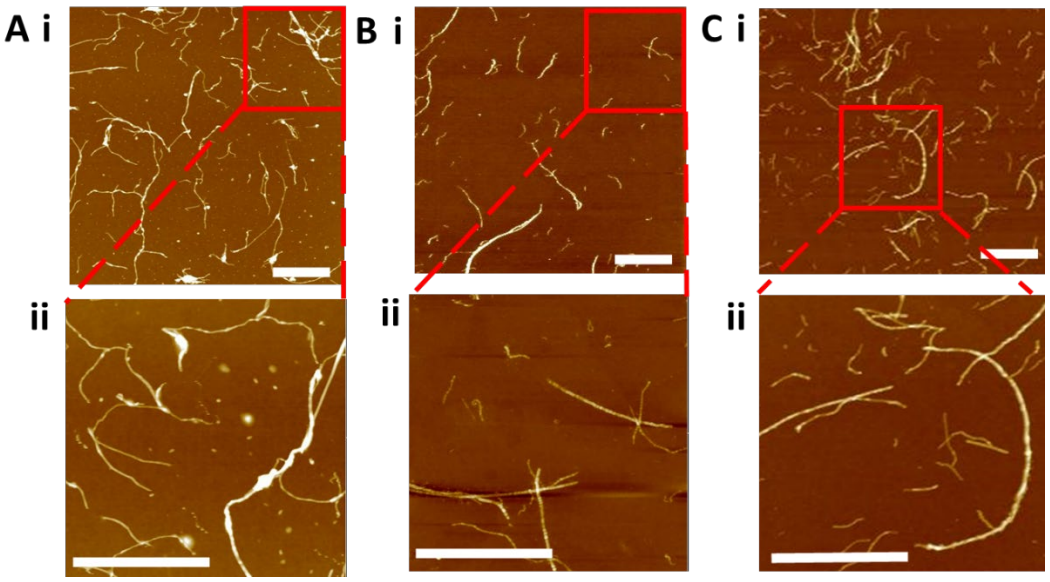

Figure 3.5 AFM images of MWNT suspended in: a) chloroform, b) 0.5% chitosan, and c) 2% BSA. The white scale bars correspond to 1 µm.

Figure 3.5 shows AFM images of the MWNT forest dispersed in chloroform, 0.5% chitosan, and 2% BSA drop casted on cleaned silicon oxide wafer. Sectional analyses show that on average, the pristine CNTs' outer diameter is 8.28 nm and increases to 10.93 nm when coated with chitosan. The MWNT's hydrophobicity causes them to bundle when suspended in solutions such as chloroform (Fig. 3.5 a). Once they are coated with polymers or proteins, such as chitosan (Fig. 3.5 b) and BSA (Fig. 3.5 c), the CNTs detangle and can suspend in aqueous solutions homogeneously. Moreover, chitosan uniformly coated the CNTs compared to BSA. Since preliminary experiments showed that only 2% BSA was able to fully disperse 800 µm long MWNTs, the 150 µm long MWNTs was used to prepare the CNT-CHIT solutions. It took approximately 2 hours of ultrasonication for the MWNTs to suspend homogeneously.

3.3.2 CNT-CHIT Electrochemical Characterization

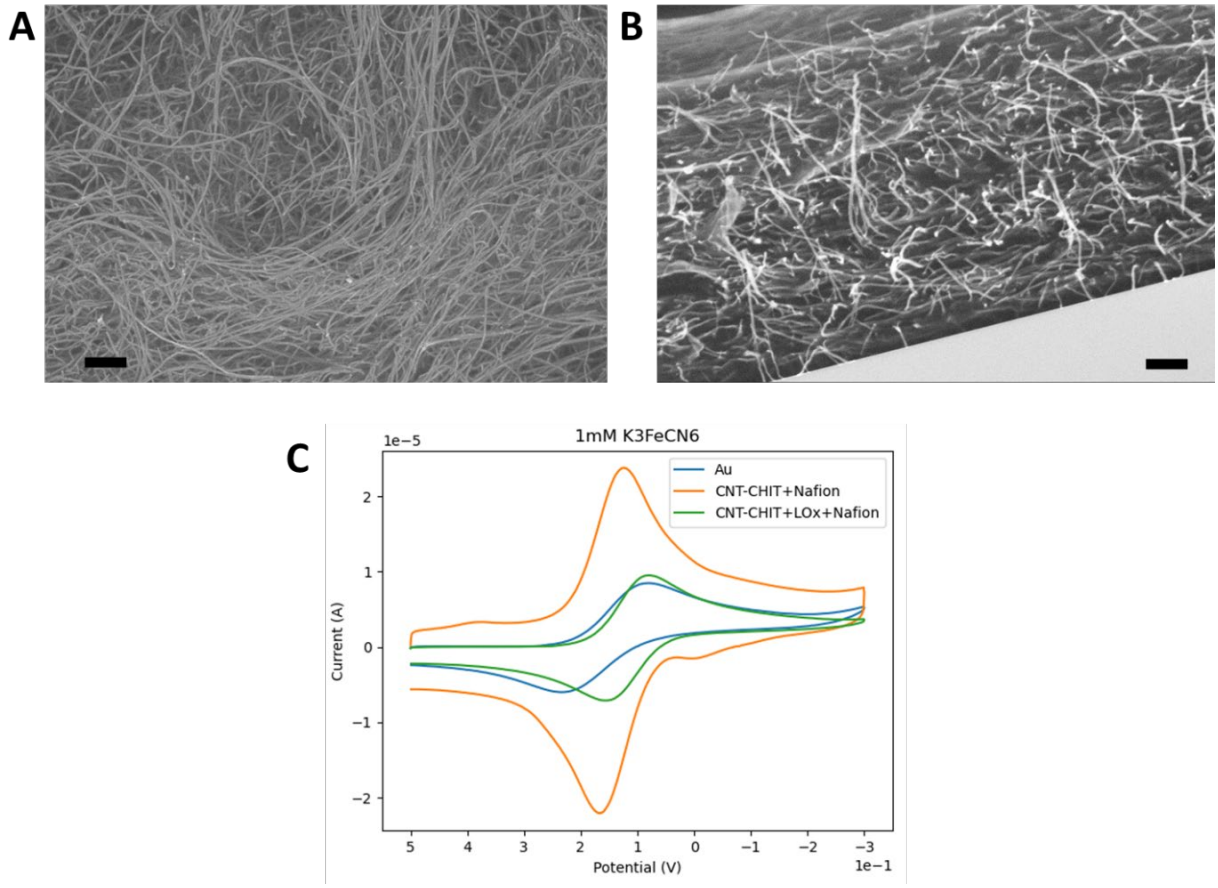

Figure 3.6 CNT-CHIT characterization - SEM images of the A) top and B) side views of the CNT-CHIT. The scale bars correspond to 200nm. C) CV of 1mM K3FeCN6 on bare Au, CNT-CHIT+Nafion, and CNT-CHIT+LOx+Nafion electrodes in PBS.

The SEM images in Fig. 3.6 a and b show that the CNT-CHIT suspension forms a highly percolated CNT network after drying under ambient conditions. The significant increase in K_3FeCN_6 redox peaks upon the addition of CNT-CHIT+Nafion on bare Au electrode (Fig. 3.6 c) indicate an increase in EASA and that the chitosan did not fully insulate the CNT surface. However, when the CNT-CHIT solution was mixed at a 1:1 ratio with LOx, the redox peaks decreased with only a slight increase compared to bare Au. The peak potential separation (ΔE_p) also decreased

from 0.150 to 0.068 and 0.044 V for bare Au, CNT-CHIT+LOx+Nafion, and CNT-CHIT+Nafion electrodes, respectively, signifying improved redox process reversibility. This phenomenon is consistently observed with other CNT covered electrodes.[49, 102] The observed decrease when the CNT-CHIT was mixed with LOx can be attributed to the reduced percolation between the individual CNTs required to form a continuous CNT network. Furthermore, preliminary tests also showed that CNT-CHIT coated gold electrode without 1% Nafion was stable in PBS. This is due to the combined effect of hydrophobic interactions between the CNT surfaces and hydrogen bonding between chitosan functional groups.[99]

3.3.3 CNT-CHIT Enzyme Matrix Performance

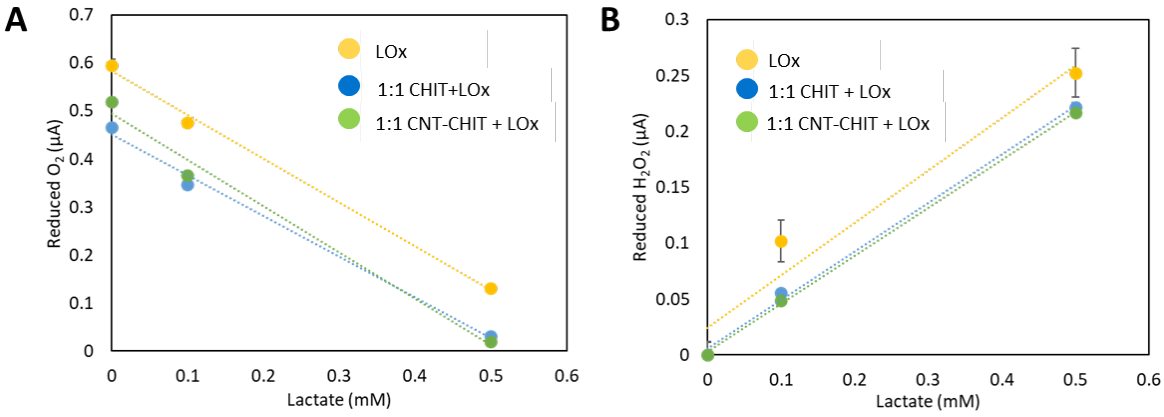

Figure 3.7 Calibration curve of LOx, 1:1 CHIT+LOx, 1:1 CNT-CHIT+LOx sensors represented as A) O_2 consumption and B) H_2O_2 production.

We evaluated the performance of the CNT matrix when integrated with LOx. All of the matrices contain equal number of enzymes and are coated with 1% Nafion. The 1:1 CHIT matrix serves as the baseline of the 1:1 CNT-CHIT matrix with the assumption that the concentration of

free chitosan is comparable. As seen in Fig. 3.7 a, the LOx matrix shows higher overall output current compared to the 1:1 CHIT+LOx and 1:1 CNT-CHIT+LOx matrices, indicating decreased O_2 flux due to the thicker enzyme matrices from the addition of chitosan polymers. This also indicates that the addition of chitosan did not form a hydrophilic membrane, which could be due to the high LOx loading. The 1:1 CNT-CHIT+LOx matrix shows slight increase in sensitivity compared to the LOx and 1:1 CHIT+LOx, enzyme matrices (Fig. 3.7). As seen in Fig. 3.5 b, many of the CNT-CHIT are shortened due to sonication, which consequently led to the ineffective formation of a conductive matrix. This is similar to the redox peaks observed in Figure 3.6 c demonstrating that the formation of a continuous CNT network within the matrix is impeded by enzyme addition. The H_2O_2 production calibration curves also exhibit similar patterns as the O_2 production (Fig. 3.7).

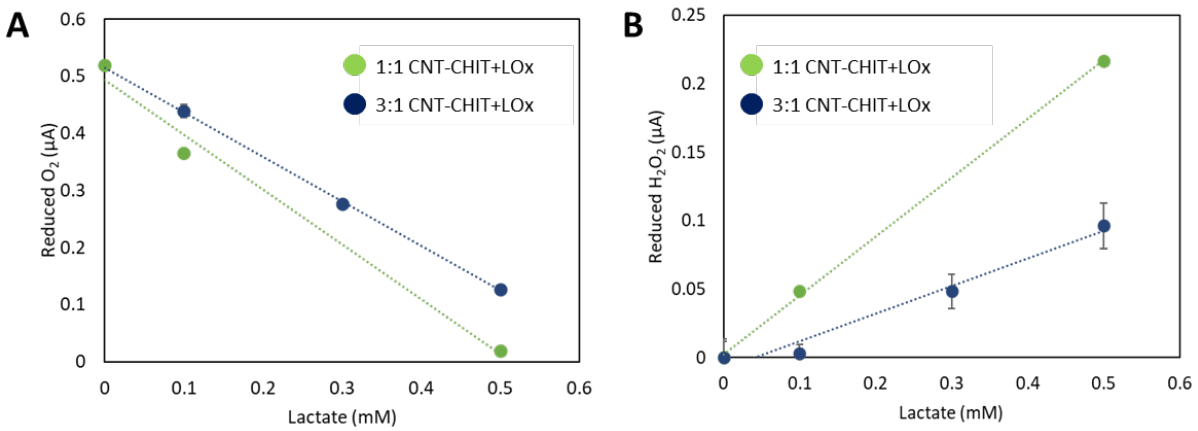

Figure 3.8 Calibration curve of 1:1 and 3:1 CNT-CHIT+LOx sensors represented as A) O_2 consumption and B) H_2O_2 production.

Based on the resulting calibration curves of 1:1 CNT-CHIT+LOx, we decided to increase the CNT ratio in the matrix to 3:1 to promote better CNT percolation. However, the 3:1 CNT-

CHIT+LOx enzyme matrix shows lower sensitivity for both O_2 consumption and H_2O_2 production with increasing lactate concentration (Fig. 3.8). One plausible explanation for this observation is that although higher ratio of CNT-CHIT lead to better CNT network formation through increased hydrophobic interactions, it also causes the matrix to be more hydrophobic. This observation is comparable to the study by Payne et al., who observed that higher SWNT-CHIT loading cause LOx crowding that prevented lactate-LOx interaction.[92] Consequently, the lactate flux decreased and was unable to reach the enzymes embedded within the matrix. Thus, there appeared to be a balance between achieving a continuous conductive CNT network whilst maintaining sufficient hydrophilicity from the chitosan.

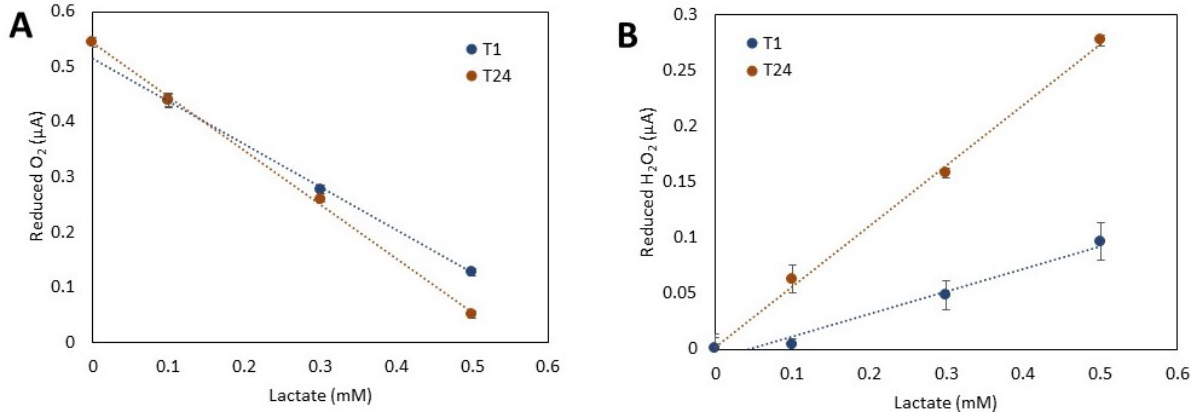

Figure 3.9 Calibration curve of 3:1 CNT-CHIT+LOx sensors represented as A) O_2 consumption and B) H_2O_2 production after 1-hour (T1) and 24-hours (T24) hydration in PBS.

Since hydrophobicity in the 3:1 CNT-CHIT+LOx sensor appeared to be the main cause of the reduced sensor sensitivity, we investigated the effect of 24-hours (T24) incubation in PBS on the sensor's performance. Similar to the results seen in chapter 1, both the O_2 consumption and H_2O_2 production sensitivity response increased at T24 (Fig. 3.9). The CNT-CHIT matrix is continuously hydrated during the 24-hour period enabling enzymes embedded deep within the

matrix to also catalyze lactate. The H_2O_2 recovery also significantly improved at T24, similar to the LOx sensors discussed in chapter 1.

Table 3-2 Summary of Lactate Sensor's Sensitivity

Enzyme Matrix	Sensitivity ($\mu A\ mM^{-1}\ cm^{-2}$)	
	Reduced O_2	Reduced H_2O_2
LOx/Nafion	-10.4	4.24
1:1 Chit: LOx/Nafion	-14.3	7.32
1:1 CNT-Chit: LOx/Nafion	-16.2	7.23
3:1 CNT-Chit: LOx/Nafion	-13.1	3.38
3:1 CNT-Chit: LOx/Nafion after 24 hydration	-16.5	9.13

Table 3-2 summarizes our lactate sensors' performance with various enzyme matrices. The data show that incorporating the CNT-CHIT to LOx at a 1:1 ratio with LOx did not significantly improve the sensor's sensitivity compared to the immobilized LOx coated with 1% Nafion. Increasing the CNT-CHIT to LOx ratio to 3:1 decreased the sensitivity due to the tighter matrix from increased hydrophobic CNT interactions but 24 hours incubation in PBS improves its performance. Our sensor performed with a comparable sensitivity compared to some representative lactate sensors (Table 3-3). However, our CNT-CHIT:LOx sensor did not perform better than the lactate sensor that sandwiched the MWNTs between the electrode and enzyme layer (LOx/pMB/MWNT).

Table 3-3 Sensor's Performance Compared to Representative Lactate Sensors

Electrode Material	**Sensitivity**		**Ref.**
	$\mu A\ mM^{-1}$	**$\mu A\ mM^{-1}\ cm^{-2}$**	
LOx-BSA-GA/Nafion/AgNp	-	0.256	89
LOx/AuNP/CNT/Gr/Pt	-	35.3	91
LOx/1-pyrenebutanoic acid succinimidyl ester/Graphene	29.9	-	77

LOx/ZnO Np/MWNT		7.3	-	76
LOx-Chit-CNT/TTF-CNT		4.8	68	92
LOx/pMB/MWNT		-	1.47×10^3	61
LOx/BSA/HRP/CHIT/FcME/MWNTs		3.42	-	93
LOx/BSA/GA		-	36.2	65
LOx/Nafion	O_2 Reduction peak	-	57.2	Ours
	Reduced O_2	-	10.4	
	Reduced H_2O_2	-	4.24	
3:1 CNT-CHIT:LOx/Nafion after 24 hours hydration	Reduced O_2	-	16.5	
	Reduced H_2O_2	-	9.12	

3.4 Conclusion

Although the CNT-CHIT polymer enhanced the bare Au's EASA, the 1:1 CNT-CHIT+LOx matrix is shown to only slightly improve the lactate sensor's sensitivity. The results indicate that the fabrication of a conductive and hydrophilic matrix depends on the optimal ratio of CNT-CHIT to LOx, which will need to be further investigated. Based on the CHIT-LOx matrix, the enzyme loading appears to be too high and prevented the formation of the hydrophilic CHIT membrane. Utilizing high MW CHIT may be able to promote better CHIT polymer interaction to form the hydrophilic membrane. The ratio of CNT to CHIT can also influence the matrix performance such that too low CHIT concentration can hinder homogenous dispersion in aqueous solution and too high CHIT concentration risks insulating the CNT surface. Various ratios of CNT to chitosan have been reported for different purposes. [49, 98, 108, 109] As previously discussed, Ghica et al., suspended 10 mg/ml of COOH-MWNT in 1% CHIT.[49] On the other hand, Mane et al. who developed a semi 3D non-enzymatic CNT-CHIT atropine sensor with single-walled CNTs utilized 0.5 mg/ml SWNT dispersed in 4% CHIT. At a fixed CHIT concentration, the output current maximized at 0.5 mg/ml

and higher concentrations over saturated the EASA.[110] Unlike their sensor, our sensor's response also relies on the biomarker's ability to permeate throughout the 3D-enzyme matrix. Therefore, the balance between CHIT and CNT must be refined and further examined. Furthermore, based on preliminary experiments, BSA was able to homogenize the CNTs faster than 1% CHIT. This is potentially because BSA can restructure and unravel its hydrophobic pockets to adhere to the CNT surface. Unlike CHIT methyl side groups, the hydrophobic pockets have a larger footprint on the CNT that allows BSA to coat the CNT surface easier than chitosan. Consequently, BSA suspended CNTs require less sonication that can also break the CNT and thus preserve the CNTs' length. This will allow the CNTs to percolate easily in the enzyme matrix compared to shorter CNTs. With the same principle, higher concentration or MW CHIT may be able to coat the CNTs easier than the current conditions and preserve the CNTs length. Ideally, the CNT-CHIT enzyme matrix should be comprised of a highly percolated CNT network capable of trapping the enzymes within the nanopores lined with CHIT.

Chapter 4 Microneedle Sensors

4.1 Background

Although recent sensors were developed with solid microneedles, one of the early MN sensors was designed with an array of hollow MNs. Jina et al., developed a CGM MN sensor comprised of 200 hollow silicon MNs that directed ISF glucose to the WE modified with GOx crosslinked with BSA (Fig. 4.1). The platform relied on the passive diffusion of ISF glucose to the WE due to the concentration gradient created from the glucose consumption on the WE. The sensor successfully monitored the ISF glucose fluctuations continuously for 72 hours with comparable results to a reference blood glucose device.[32] While Jina et al. demonstrated that passive diffusion enabled continuous monitoring, the sensor operation required manual PBS addition to the platform. Thus, ISF extraction is a big challenge that must be resolved.

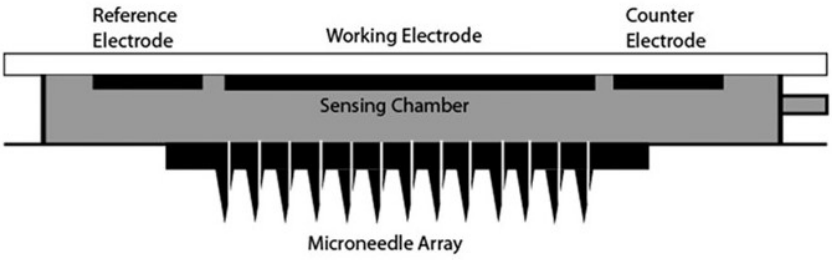

Figure 4.1 Schematic of the glucose sensor with hollow microneedle array. [32] Reproduced with permission.

As mentioned in chapter 1, there are multiple extraction mechanisms explored for ISF extraction. Samant and Prausnitz reported that with capillary force, 0.01 – 003 µL of ISF was extracted by a single MN with 108 – 260 µm inner diameter after 20 minutes. Through osmotic pressure, a 10 MN patch coated with 20 µg of maltose collected 0.0056 µL of ISF per micropore within 20 minutes, compared to non-coated MN at 0.0006 µL. The maltose coating dissolved in

a pig skin model that increased the ionic strength in the MN lumen and created a 2.2 kPa pressure difference to promote osmotic driven flow. However, it was reported that the best technique to extract ISF is through pressure-driven convection that can be achieved through either introducing a negative pressure at the micropore sites or positive pressure on the skin surface. With a -85 kPa suction pressure, the 10 MN patch extracted 0.0064 µL per pore of ISF but the high negative pressure caused the pores to collapse. When the skin was curved, the pores opened and the amount of ISF extracted increased to 0.03 – 0.47 µL per pore. The application of positive pressure, approximately 25 kPa below the skin, by pinching the nearby skin also extracted a high volume of ISF per pore at 0.16 µL per pore. To ensure that a sufficient amount of ISF is extracted, they designed a 50 MN array steel patch and when suction was applied for 20 minutes, 2.3 µL ISF was collected per person. Therefore, pressure-driven convection is the most efficient technique of ISF extraction through hollow MNs by creating a large pressure drop across the dermis. [31]

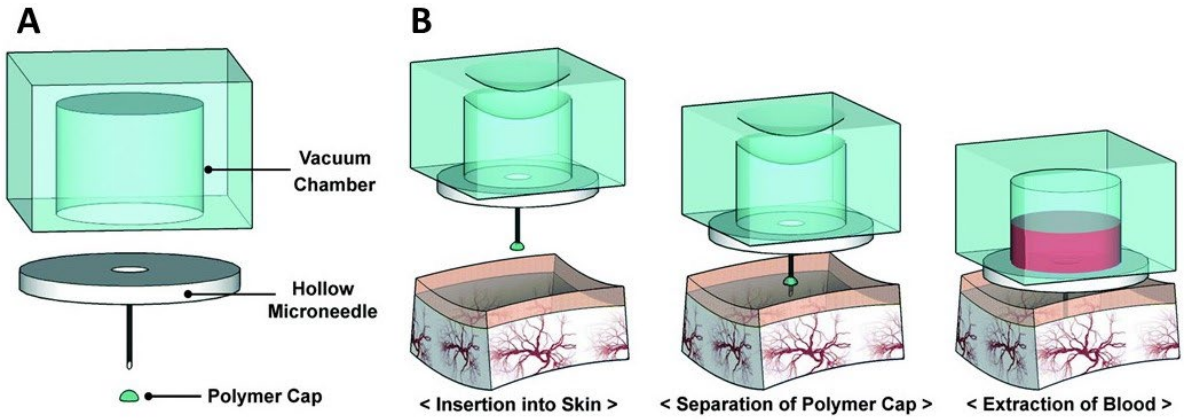

Figure 4.2 Schematics of the pre-vacuumed PDMS MN platform A) blood extraction system comprised of a vacuum chamber and hollow microneedle capped with polymer B) operation principle whereby a one-touch press simultaneously caused microneedle insertion into the skin. [111]Reproduced with permission.

Subsequently many MN platforms implemented the pressure-driven convection technique, particularly the application of a negative pressure in the chamber, to extract sufficient volume of ISF. Crosslinked PDMS is a popular material for fabricating the MN chamber systems for its ease of use to fabricate various structures and water impermeability, among others. The Slygard 184 by DOWSIL is the most prevalent silicone elastomer used for lab-on-chip devices.[112] The previously discussed multiplexed glucose and cholesterol sensor made a PDMS touch-switch that was placed over the microneedle for blood extraction (Fig. 1.3 b). When the PDMS touch-switch was pushed, the single MN with a 60 μm inner diameter single extracted 30 ± 5 μL of blood from a rabbit in 10 seconds.[27] The same group also designed a similar MN platform with a pre-vacuumed PDMS chamber that eased the blood extraction. The pre-vacuumed PDMS chamber and microneedle were sealed with parylene coating and capped with polymer, respectively, to maintain the vacuum potential for a long time (Fig. 4.2). This technique allowed a more consistent volume extraction. Tests demonstrated that the volume extracted positively correlate with increasing vacuum chamber size. The platform extracted more distilled water than blood with the same sized PDMS chamber due to the higher viscosity of blood. The pre-vacuumed PDMS chamber successfully collected up to 31.3 ± 2 μL blood in a 5 mm diameter chamber from a rabbit.[111] The PDMS chambers used in these two studies were fabricated with a 10:1 (v/v) ratio of the Slygard 184 elastomer to curing agent. In this chapter we will describe the development of a wearable PDMS-based lactate sensor and investigate its performance for extracting water and ISF mimicking fluid.

4.2 Materials and Methods

4.2.1 Materials

Slygard 184 Silicone Elastomer was manufactured by Dow Corning (USA). The microneedles were from 3M Canada and were originally made for transdermal drug delivery. The Teflon molds were custom made by the Science Technical Services at University of Waterloo. Glycerol (99.5% GC) was obtained from EMD Millipore (Merck, Darmstadt, Germany). The glue used to adhere the PDMS pieces was manufactured by Krazy Glue (USA). The petri dishes were manufactured by Fisher Scientific (Canada). The scalpel knife #11 were manufactured by Swann Morton (Sheffield, England).

4.2.2 PDMS Chamber Fabrication and Testing

Slygard 184 was used to make the PDMS chamber by mixing the curing agent to elastomer at 1:10 and 1:30 ratio. The mixture was homogeneously mixed and placed in a vacuum chamber to remove the bubbles before pouring it on custom made Teflon molds. The MN array was placed in the MN piece mold to ensure that the PDMS forms a right seal around the MN. The mixture was degassed again to remove the remaining bubbles. It was then left to cure overnight at 85^{o}C. The cured PDMS were removed from the Teflon mold using scalpel blades and excess PDMS were cut off. The chamber and microneedle sections of the PDMS chamber were adhered together using Krazy Glue. Extraction experiments were conducted on a 35 x 10 mm petri dish. The PDMS chamber was suspended above the solution filled dish using glass slides.

4.3 Results and Discussions

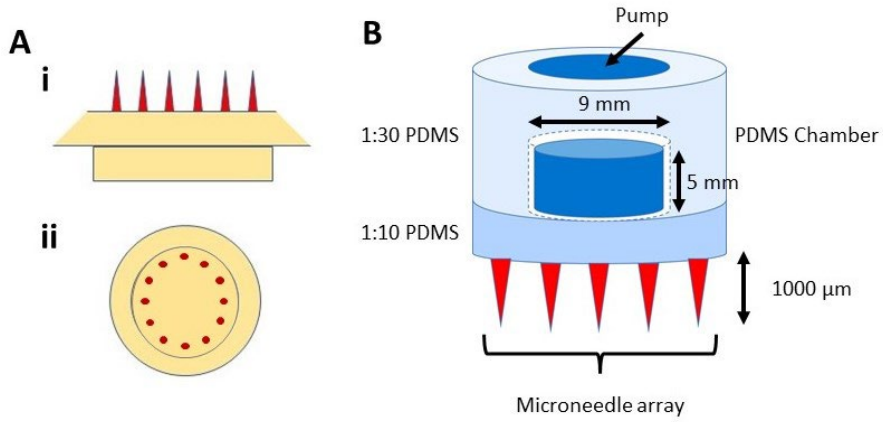

Figure 4.3 Schematic of the A) microneedle array comprised of 12 1000 µm long microneedles with 80 µm lumen from the (i) side and (ii) top view B) PDMS microneedle platform.

The microneedle array is comprised of 12 hollow microneedles arranged in a circle with a length of 1000 µm and inner lumen of 80 µm (Fig. 4.3 a). The PDMS chamber is consisted of two parts, the chamber and microneedle section, fabricated with different PDMS to curing agent ratio. Preliminary tests only utilized the standard 1:10 ratio of curing agent to elastomer but the fabricated PDMS chamber extracted low volumes of solution with each pump. Therefore, we decreased the ratio to 1:30 to form a PDMS with lower elastic modulus (λ). Based on Wang et al.'s study, the lower degree of crosslinking produces a softer PDMS than higher degree of crosslinking. The experimental λ for a 1:10 and 1:33 PDMS were measured to be 2.61 MPa and 0.56 MPa, respectively. This is caused by higher crosslinking associated with higher concentration of curing agent.[113] Thus, we used the 1:30 PDMS to fabricate the chamber section because higher PDMS deformation will promote higher volumes of solution extracted (Fig. 4.3 b). Since the microneedle section require strong structural integrity and must exhibit minimal deformation during pumping, a 1:10 PDMS ratio was used (Fig. 4.3 b). Krazy glue was used to adhere both

sections of the PDMS chamber. The inner chamber has a diameter of 9 mm and height of 5 mm with a volume of 500 µL.

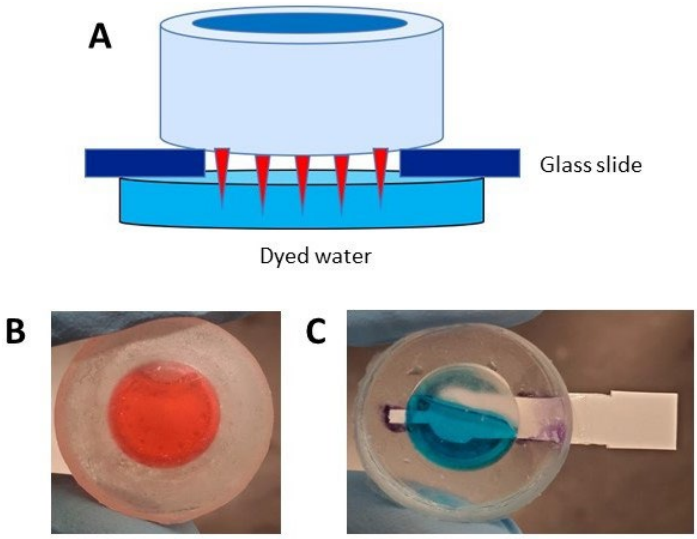

Figure 4.4 PDMS Chamber solution extraction experiment: A) schematic of the experimental set up, B) 45% glycerol solution, and C) solution extraction of assembled transdermal sensor.

We placed the PDMS chamber on glass sides above a petri dish contained with solution to assess its ability to extract solutions (Fig. 4.4 a). The initial test was conducted on water dyed with food coloring without the presence of the sensor and the PDMS chamber was ≥ 95% filled with 5-6 full pumps. Similar test was conducted when the chamber was pre-filled with water with comparable result. In real-life applications, the chamber will be filled with buffer to mix with the ISF/blood since forced gas in the skin can cause detrimental effects. Since the MN length are 1000 µm, it will penetrate through the dermis and extract both ISF and capillary blood. Therefore, the solution extracted will have a higher viscosity than water and/or PBS. PBS possess a viscosity of 0.7 cP at 37C versus 4.4 cP for blood and so a 45% glycerol solution that mimics the blood's viscosity was used.[65] The PDMS chamber also filled ≥ 95% of the chamber with 45% glycerol after

5-6 pumping (Fig. 4.4 b). When a flexible sensor strip was placed in the chamber, some of the microneedles were blocked that hindered effective solution extraction and mixing. Consequently, the chamber was approximately 60% filled at 300 µL (Fig. 4.4 c). Overall, the fabricated PDMS chamber successfully extracted larger volume of solutions compared to Li et al.'s studies, sufficient for biomarker monitoring.

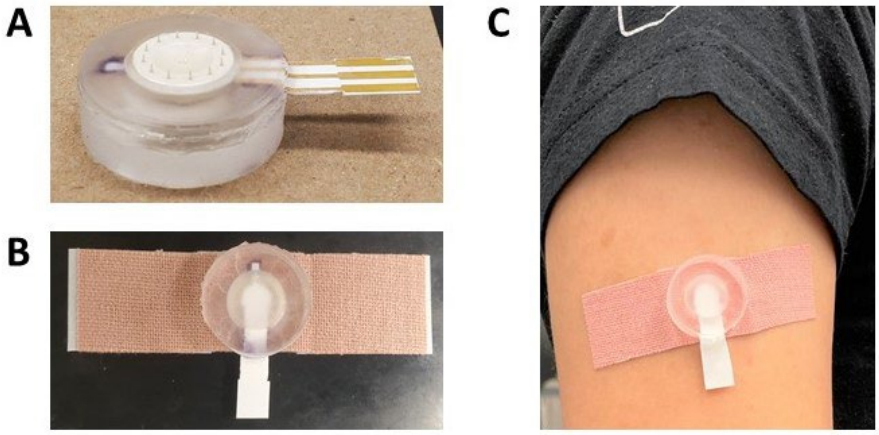

Figure 4.5 Photographs of the A) assembled transdermal microneedle sensor, B) transdermal sensor mounted on medical bandage, and C) the fully assembled transdermal sensor worn on the skin.

The assembled PDMS chamber is illustrated in Fig 4.5 a, complete with the sensor strip sandwiched between the two PDMS sections. It was then mounted on a medical bandage to stabilize the sensor on the skin as illustrated in Fig. 4.5 b & c.

4.4 Conclusion

We demonstrated the fabrication of a wearable MN sensor with PDMS chamber. The platform utilizes a pressure-driven convection technique by designing a pumping mechanism on the top of the PDMS chamber. It successfully extracted up to 500 µL of solution, including solution

with viscosity comparable to whole blood, with 5-6 pumping. The chamber was only filled to 60% of its full capacity when a sensor strip placed in the chamber, which prevented effective solution mixing and extraction. Overall, the fabricated PDMS chamber is a promising MN platform but further studies must be conducted to evaluate whether diffusion will ensure that the solution in the chamber reflect the biomarker concentrations in ISF. Our previous study demonstrated that solution could pass through the microneedles under positive pressure.[65] However, since the platform is a closed system, the mass transport of biomarkers will solely be due to molecular diffusion, similar to what Jina et al. observed. Furthermore, in addition to evaluating the platform's long-term stability, the potential effects of fouling that can block the microneedle lumen must be evaluated.

Chapter 5 Conclusion

Wearable biosensors for continuous monitoring are highly desired to improve disease prognosis. Interstitial fluid, easily accessible through the skin, is an attractive minimally invasive surrogate biofluid to blood for its comparable composition and direct circulation with blood. One of the clinically important biomarkers not often targeted is lactate. It is an important predictive biomarker for pressure ischemia and predicting mortality in surgical patients. Our lab previously developed a wearable transdermal lactate sensor consisting of an array of microneedles, a flexible three electrode electrochemical system and a crosslinked LOx bioreceptor. I aimed to improve upon this sensor by integrating carbon nanotubes and fabricating a wearable transdermal sensor platform.

In chapter 2 I demonstrated that the non-covalent method of enzyme immobilization technique with Nafion coating retained the most enzyme activity compared to the covalent crosslinking technique and was stable for 24 hours. Unlike other oxidase-based sensors that utilize PB as a redox mediator, we observed both O_2 consumption and H_2O_2 production as lactate concentration increased. Enzyme hydration increased the overall output current but only increased the sensitivity of H_2O_2 production by activating more enzymes and increasing O_2 flux. The lactate sensor also has a linear range of 0 – 500 mM, a concentration range more suited for sweat lactate sensor. Some studies extended the sensor's linear range by using diffusion layers at the expense of the sensor's sensitivity. There are also other studies that have a large linear range by using CHIT membranes or crosslinked strategies. However, to date, there are no systematic studies that explores the factors that affects enzyme K_m. Understanding how enzymes

structural changes, product buildup, and other factors influences the sensor's K_m can enable a more strategic enzyme immobilization for sensor development.

In chapter 3 I investigated the effects of integrating CNT-CHIT into the LOx enzyme matrix. The lower O_2 flux from the CHIT-LOx matrix results suggests that the hydrophilic CHIT membrane did not form effectively due to the high LOx loading. Decreasing the LOx loading and utilizing high MW CHIT can potentially resolve this issue. The CNT-CHIT matrix was shown to increase the EASA for K_3FeCN_6 redox processes but addition of enzyme decreased the redox current due to reduced CNT percolation required to generate a conductive matrix. The 1:1 CNT-CHIT+LOx matrix only slightly improved the O_2 reduction in lactate but increasing the CNT-CHIT to LOx ratio to 3:1 decreased the sensor's sensitivity. This can be attributed to the increased matrix hydrophobicity such that after overnight hydration in PBS the O_2 consumption and H_2O_2 production sensitivity increased. These results indicate poor CNT-CHIT-LOx matrix formation due to the shortened CNT-CHIT after sonication. Decreasing the CNT concentration and/or using high MW CHIT may better generate a homogenous suspension with long CNT-CHIT to form the ideal conductive matrix. These results suggest that the CNT-CHIT and CNT-CHIT to LOx ratio must be optimized to generate a conductive, sufficiently porous, and hydrophilic matrix.

In chapter 4, I showed the fabrication of a wearable PDMS microneedle sensor platform that was able to extract up to 500 µL of a glycerol solution with a viscosity similar to blood. The principle of solution extraction relied on the generation of a large pressure drop across the skin through the pump located on the top of the chamber. The PDMS chamber was made of two parts, the chamber with pump and microneedle sections, made with 1:30 and 1:10 ratio of curing agent to elastomer. The chamber with pump was made with 1:30 PDMS because the 1:10 PDMS pump

did not deform sufficiently to extract solutions. The PDMS chamber should be further assessed for its implementation in continuous monitoring. Understanding how diffusion affect the accuracy and timely monitoring is beneficial to determining if hollow MNs are advantageous to solid MNs.

These studies provided more insight on the development of wearable ISF sensors in terms of enzyme immobilization, nanomaterial integration, and MN based platform fabrication. However, there are many aspects that must be further investigated. I recommend the following research objectives:

1. We have discussed that the limited sensor linear range is a common issue. However, there are no studies that systematically investigates how factors such as structural changes and product buildup affect the linear range. For instance, the charge on the membrane may cause product build up through electrostatic interactions. This is an important parameter for monitoring ISF biomarkers because the concentrations of some biomarkers are in the high mM levels. In fact, some biomarkers such as skin cancer that are unique to skin ISF are localized, making the ISF levels higher than the blood levels.
2. Even though the LOx imparts selectivity on the sensor, ISF and blood are rich in biomarkers that may have some cross reactivity with the enzyme. Therefore, sensor's selectivity towards lactate in the presence of interfering molecules such as ascorbic acid, uric acid, and glucose must be evaluated. This is an important parameter that can affect the sensor's performance in complex biofluid. This parameter can be tested by measuring the output signal after successive addition of interfering molecules before the sensor performance is evaluated in interstitial fluid or blood mimicking fluid.

3. The sensor's ability to detect the fluctuations in lactate concentrations should be tested after 24 hours of hydration. The output signal must be reproducible to enable continuous monitoring, which determines the sensor's accuracy in determining unknown concentration of lactate. Many studies have previously reported unstable output signal due to enzyme leaching or denaturation, which consequently requires the sensor to be recalibrated every time it is used. The appropriate mitigation approach, (e.g. recalibration) will be implemented depending on the sensor's output signal stability.
4. The microneedles used here are 1000 µm long that can also penetrate through the capillaries and extract a mixture of blood and IF. Since studies that are exploring the clinical significance of ISF biomarkers focus on ISF, the microneedles used should be shortened to 800 µm to ensure only ISF extraction. ISF also do not contain clotting factors that should promote long-term stability and performance. Shorter MNs also significantly reduces the risk of penetrating skin nerves, making it less painful. Therefore, ISF sensor platforms should be designed with MNs that are at maximum 800 µm.
5. The characteristics of CNT-CHIT matrix is still not yet fully understood. We observed that the 1:1 CNT-CHIT+LOx did not significantly improve the enzyme performance compared to CHIT+LOx matrix. Increasing the CNT-CHIT to LOx ratio from 1:1 to 3:1 increased the hydrophobicity of the matrix, which subsequently reduced the biomarker flux and decreased sensitivity. However, this was conducted with only 1% CHIT coated CNT. Increase in CHIT concentration and/or high MW CHIT can promote CHIT aggregation, to create hydrophilic nanopores in the matrix and promote higher biomarker flux. Therefore, a systematic study of the CNT-CHIT and CNT-CHIT+LOx ratio is needed and can shed light

on nanomaterial composites for not only biosensor applications but other material science advancements. Furthermore, although the dried CNT-CHIT matrix produced a highly percolated CNT network, the SEM images showed a densely packed CNT matrix. Creating a porous structure through techniques such as freeze drying may improve the sensor's performance.

6. The sensor's long-term safety must be studied. While the MNs are biocompatible since they were originally designed for drug delivery, the body will be exposed to exogenous materials such as CNTs and LOx. Although the Nafion was shown to be stable for within 24 hours, it was conducted in a lab-controlled environment with minimal mechanical disruptions. Another safety concern is microneedle breakage that may leave embedded parts in the skin and cause adverse effects. So, in vitro safety tests as well as the immune response must be evaluated before in vivo experiments are conducted.
7. Lastly, in vivo experiments are needed to realize and evaluate the sensor's performance as a wearable sensor. The study will shed light on the effect of body movement, physiological processes, and temperature on the sensor's ability to generate stable output signal while worn on the skin over a period of time. The effect of biofluid on the mass transfer of lactate through the microneedles and activities that induce fluctuations in lactate levels will also be obtained through in vivo study. A reference technique, such as a commercial hand-held lactate meter, should be used to determine the sensor's accuracy.

References

1. Cardiovascular Diseases (CVDs). who.int/en/news-room/fact-sheets/detail/ cardiovascular-diseases-(cvds). (2021)

2. Diabetes Facts and Figures. idf.org/aboutdiabetes/what-is-diabetes/facts-figures.html. (2021)

3. COVID-19 Dashboard by the Center for Systems Science and Engineering (CSSE) at Johns Hopkins University (JHU). coronavirus.jhu.edu/map.html. (2022)

4. Inamdar, A. A. & Inamdar, A. C. Heart Failure: Diagnosis, Management and Utilization. *J Clin Med* **5** (2016).

5. Bansal, N. Prediabetes diagnosis and treatment: A review. *World J Diabetes* **6**, 296-303 (2015).

6. Raja, J. M. *et al*. Apple Watch, Wearables, and Heart Rhythm: where do we stand? *Anna Transl Med* **7**, 417 (2019).

7. Seshadri, D. R. *et al*. Accuracy of Apple Watch for Detection of Atrial Fibrillation. *Circulation* **141**, 702-703 (2020).

8. Isakadze, N. & Martin, S. S. How useful is the smartwatch ECG? *Trends Cardiovasc Med* (2019).

9. Facchinetti, A., Del Favero, S., Sparacino, G. & Cobelli, C. Model of glucose sensor error components: identification and assessment for new Dexcom G4 generation devices. *Med Biol Eng Comput* **53**, 1259-1269 (2015).

10. Heinemann, L. *et al*. Real-time continuous glucose monitoring in adults with type 1 diabetes and impaired hypoglycaemia awareness or severe hypoglycaemia treated with multiple daily insulin injections (HypoDE): a multicentre, randomised controlled trial. *Lancet* **391**, 1367-1377 (2018).

11. Dervisevic, M., Alba, M., Prieto-Simon, B. & Voelcker, N. H. Skin in the diagnostics game: Wearable biosensor nano- and microsystems for medical diagnostics. *Nano Today* **30**, 100828 (2020).

12. Bariya, M., Nyein, H. Y. Y. & Javey, A. Wearable sweat sensors. *Nat Electron* **1**, 160-171 (2018).

13. Lee, H. *et al*. Wearable/disposable sweat-based glucose monitoring device with multistage transdermal drug delivery module. *Sci Adv* **3**, e1601314 (2017).

14. Wang, R., Zhai, Q., An, T., Gong, S. & Cheng, W. Stretchable gold fiber-based wearable textile electrochemical biosensor for lactate monitoring in sweat. *Talanta* **222**, 121484 (2021).

15. Bandodkar, A. J. *et al*. Battery-free, skin-interfaced microfluidic/electronic systems for simultaneous electrochemical, colorimetric, and volumetric analysis of sweat. *Sci Adv* **5**, eaav3294 (2019).

16. Sekine, Y. *et al*. A fluorometric skin-interfaced microfluidic device and smartphone imaging module for in situ quantitative analysis of sweat chemistry. *Lab Chip* **18**, 2178-2186 (2018).

17. Kim, J. *et al*. Simultaneous Monitoring of Sweat and Interstitial Fluid Using a Single Wearable Biosensor Platform. *Adv Sci* **5**, 1800880 (2018).

18. Roustit, M., Blaise, S. & Cracowski, J. Trials and tribulations of skin iontophoresis in therapeutics. *Br J Clin Pharmacol* **77**, 63-71 (2014).

19. Kim, J., Campbell, A. S., de Ávila, B. E. & Wang, J. Wearable biosensors for healthcare monitoring. *Nat Biotechnol* **37**, 389-406 (2019).

20. Emaminejad, S. *et al*. Autonomous sweat extraction and analysis applied to cystic fibrosis and glucose monitoring using a fully integrated wearable platform. *Proc Natl Acad Sci USA* **114**, 4625 (2017).

21. Lim, T. *et al*. Human sweat monitoring using polymer-based fiber. *Sci Rep* **9**, 1-8 (2019).

22. Scallan, J., Huxley, V. H. & Korthuis, R. J. in *The Interstitium* (Morgan & Claypool Life Sciences, 2010).

23. Samant, P. P. *et al*. Sampling interstitial fluid from human skin using a microneedle patch. *Sci Transl Med* (2020).

24. Stewart, R. H. A Modern View of the Interstitial Space in Health and Disease. *Front Vet Sci* **0** (2020).

25. Cengiz, E. & Tamborlane, W. V. A Tale of Two Compartments: Interstitial Versus Blood Glucose Monitoring. *Diabetes Technol & Ther* **11 Suppl 1**, S11-16 (2009).

26. Ahn, S. & Simpson, R. J. Body fluid proteomics: Prospects for biomarker discovery. *PROTEOMICS Clin Appl* **1**, 1004-1015 (2007).

27. Li, C. G. *et al*. One-touch-activated blood multidiagnostic system using a minimally invasive hollow microneedle integrated with a paper-based sensor. *Lab Chip* **15**, 3286-3292 (2015).

28. Goud, K. Y. *et al*. Wearable Electrochemical Microneedle Sensor for Continuous Monitoring of Levodopa: Toward Parkinson Management. *ACS Sens* **4**, 2196-2204 (2019).

29. Chen, Y. *et al*. Skin-like biosensor system via electrochemical channels for noninvasive blood glucose monitoring. *Sci Adv* **3**, e1701629 (2017).

30. Liu, G. *et al*. Microneedles for transdermal diagnostics: Recent advances and new horizons. *Biomaterials* **232**, 119740 (2020).

31. Samant, P. P. & Prausnitz, M. R. Mechanisms of sampling interstitial fluid from skin using a microneedle patch. *Proc Natl Acad Sci USA* **115**, 4583 (2018).

32. Jina, A. *et al*. Design, Development, and Evaluation of a Novel Microneedle Array-based Continuous Glucose Monitor. *J Diabetes Sci Technol* **8**, 483-487 (2014).

33. Ciui, B. *et al*. Wearable Wireless Tyrosinase Bandage and Microneedle Sensors: Toward Melanoma Screening. *Adv Healthc Mater* **7**, 1701264 (2018).

34. Sharma, S. *et al*. A pilot study in humans of microneedle sensor arrays for continuous glucose monitoring. *Anal Methods* **10**, 2088-2095 (2018).

35. Bal, S. M., Caussin, J., Pavel, S. & Bouwstra, J. A. In vivo assessment of safety of microneedle arrays in human skin. *Eur J Pharm Sci* **35**, 193-202 (2008).

36. Phypers, B. & Pierce, J. T. Lactate physiology in health and disease. *Continuing Education in Anaesthesia Critical Care & Pain* **6**, 128-132 (2006).

37. Krogstad, A. L., Jansson, P. -., Gisslén, P. & Lönnroth, P. Microdialysis methodology for the measurement of dermal interstitial fluid in humans. *Br J Dermatol* **134**, 1005-1012 (1996).

38. Rassaei, L., Olthuis, W., Tsujimura, S., Sudhölter, E. J. R. & van den Berg, A. Lactate biosensors: current status and outlook. *Anal Bioanal Chem* **406**, 123-137 (2014).

39. Shapiro, N. I. *et al*. Serum Lactate as a Predictor of Mortality in Emergency Department Patients with Infection. *Ann Emerg Med* **45**, 524-528 (2005).

40. Derbyshire, P., Barr, H., Davis, F. & Higson, S. Lactate in human sweat: a critical review of research to the present day. *J Physiol Sci* **62**, 429-440 (2012).

41. Van Hoovels, K. *et al*. Can Wearable Sweat Lactate Sensors Contribute to Sports Physiology? *ACS Sens* **6**, 3496-3508 (2021).

42. Grassi, B., Quaresima, V., Marconi, C., Ferrari, M. & Cerretelli, P. Blood lactate accumulation and muscle deoxygenation during incremental exercise. *J Appl Physiol* **87**, 348-355 (1999).

43. Spehar-Délèze, A., Anastasova, S. & Vadgama, P. Monitoring of Lactate in Interstitial Fluid, Saliva and Sweat by Electrochemical Biosensor: The Uncertainties of Biological Interpretation. *Chemosensors* **9** (2021).

44. Ming, D. K. *et al*. Real-time continuous measurement of lactate through a minimally invasive microneedle patch: a phase I clinical study. *BMJ Innov* **8**, 87 (2022).

45. Bard, Allen J., Faulkner, Larry R. *Electrochemical Methods: Fundamentals and Applications.* 1 -387 (Wiley, United States of America, 2001).

46. Zhu, X. *et al*. Water Splitting-Assisted Electrocatalytic Oxidation of Glucose with a Metal–Organic Framework for Wearable Nonenzymatic Perspiration Sensing. *Anal Chem* **91**, 10764-10771 (2019).

47. Mondal, S. & Subramaniam, C. Point-of-Care, Cable-Type Electrochemical Zn2+ Sensor with Ultrahigh Sensitivity and Wide Detection Range for Soil and Sweat Analysis. *ACS Sustain Chem Eng* **7**, 14569-14579 (2019).

48. Elgrishi, N. *et al*. A Practical Beginner's Guide to Cyclic Voltammetry. *J Chem Educ* **95**, 197-206 (2018).

49. Ghica, M. E., Pauliukaite, R., Fatibello-Filho, O. & Brett, C. M. A. Application of functionalised carbon nanotubes immobilised into chitosan films in amperometric enzyme biosensors. *Sens Actuators B Chem* **142**, 308-315 (2009).

50. Zhao, Y. *et al*. Highly Stretchable and Strain-Insensitive Fiber-Based Wearable Electrochemical Biosensor to Monitor Glucose in the Sweat. *Anal Chem* **91**, 6569-6576 (2019).

51. Zhu, X., Ju, Y., Chen, J., Liu, D. & Liu, H. Nonenzymatic Wearable Sensor for Electrochemical Analysis of Perspiration Glucose. *ACS Sens* **3**, 1135-1141 (2018).

52. Bae, C. W. *et al*. Fully Stretchable Capillary Microfluidics-Integrated Nanoporous Gold Electrochemical Sensor for Wearable Continuous Glucose Monitoring. *ACS Appl Mater Interfaces* **11**, 14567-14575 (2019).

53. Lee, H. *et al*. A graphene-based electrochemical device with thermoresponsive microneedles for diabetes monitoring and therapy. *Nat Nanotechnol* **11**, 566-572 (2016).

54. Tîlmaciu, C. & Morris, M. C. Carbon nanotube biosensors. *Front Chem* **0** (2015).

55. Putzbach, W. & Ronkainen, N. J. Immobilization Techniques in the Fabrication of Nanomaterial-Based Electrochemical Biosensors: A Review. *Sensors* **13** (2013).

56. Wang, J. Carbon-Nanotube Based Electrochemical Biosensors: A Review. *Electroanalysis* **17**, 7-14 (2005).

57. Veetil, J. V. & Ye, K. Development of Immunosensors Using Carbon Nanotubes. *Biotechnol Prog* **23**, 517-531 (2007).

58. Eatemadi, A. *et al*. Carbon nanotubes: properties, synthesis, purification, and medical applications. *Nanoscale Res Lett* **9**, 393 (2014).

59. Bonaventura, J. M. *et al*. Reliability and accuracy of six hand-held blood lactate analysers. *J Sports Sci Med* **14**, 203-214 (2015).

60. Crotty, N. M., Boland, M., Mahony, N., Donne, B. & Fleming, N. Reliability and Validity of the Lactate Pro 2 Analyzer. *Meas Phys Educ Exerc Sci* **25**, 202-211 (2021).

61. Bollella, P., Sharma, S., Cass, A. E. G. & Antiochia, R. Microneedle-based biosensor for minimally-invasive lactate detection. *Biosens Bioelectron* **123**, 152-159 (2019).

62. Xuan, X., Pérez-Ràfols, C., Chen, C., Cuartero, M. & Crespo, G. A. Lactate Biosensing for Reliable On-Body Sweat Analysis. *ACS Sens* **6**, 2763-2771 (2021).

63. Tur-García, E. L. *et al*. Novel flexible enzyme laminate-based sensor for analysis of lactate in sweat. *Sens Actuators B Chem* **242**, 502-510 (2017).

64. Thomas, N., Lähdesmäki, I. & Parviz, B. A. A contact lens with an integrated lactate sensor. *Sens Actuators B Chem* **162**, 128-134 (2012).

65. Wang, Y., Ausri, I. R., Wang, Z., Derry, C. & Tang, X. Towards A Transdermal Membrane Biosensor for the Detection of Lactate in Body Fluids. *Sens Actuators B Chem* **308**, 127645 (2020).

66. Khatami, S. H. *et al*. Glucose oxidase: Applications, sources, and recombinant production. *Biotechnol App Biochem* (2021).

67. Azevedo, A. M., Prazeres, D. M. F., Cabral, J. M. S. & Fonseca, L. P. Ethanol biosensors based on alcohol oxidase. *Biosens Bioelectron* **21**, 235-247 (2005).

68. Hiraka, K. *et al*. Minimizing the effects of oxygen interference on l-lactate sensors by a single amino acid mutation in Aerococcus viridans l-lactate oxidase. *Biosens Bioelectron* **103**, 163-170 (2018).

69. Teymourian, H. *et al*. Microneedle-Based Detection of Ketone Bodies along with Glucose and Lactate: Toward Real-Time Continuous Interstitial Fluid Monitoring of Diabetic Ketosis and Ketoacidosis. *Anal Chem* **92**, 2291-2300 (2020).

70. Wang, J. Electrochemical Glucose Biosensors. *Chem Rev* **108**, 814-825 (2008).

71. Karyakin, A. A., Karyakina, E. E. & Gorton, L. The electrocatalytic activity of Prussian blue in hydrogen peroxide reduction studied using a wall-jet electrode with continuous flow. *J Electroanal Chem* **456**, 97-104 (1998).

72. Liu, Y., Yu, Q., Luo, X., Yang, L. & Cui, Y. Continuous monitoring of diabetes with an integrated microneedle biosensing device through 3D printing. *Microsyst Nanoeng* **7**, 1-12 (2021).

73. Cinti, S., Arduini, F., Moscone, D., Palleschi, G. & Killard, A. J. Development of a Hydrogen Peroxide Sensor Based on Screen-Printed Electrodes Modified with Inkjet-Printed Prussian Blue Nanoparticles. *Sensors* **14** (2014).

74. Sassolas, A., Blum, L. J. & Leca-Bouvier, B. D. Immobilization strategies to develop enzymatic biosensors. *Biotechnol Adv* **30**, 489-511 (2012).

75. Migneault, I., Dartiguenave, C., Bertrand, M. J. & Waldron, K. C. Glutaraldehyde: behavior in aqueous solution, reaction with proteins, and application to enzyme crosslinking. *BioTechniques* **37**, 790-802 (2004).

76. Wang, Y. T. *et al*. A novel l-lactate sensor based on enzyme electrode modified with ZnO nanoparticles and multiwall carbon nanotubes. *J Electroanal Chem* **661**, 8-12 (2011).

77. Labroo, P. & Cui, Y. Flexible graphene bio-nanosensor for lactate. *Biosens Bioelectron* **41**, 852-856 (2013).

78. Zhu, Z. *et al*. Nano-yarn carbon nanotube fiber based enzymatic glucose biosensor. *Nanotechnology* **21**, 165501 (2010).

79. Kusoglu, A. & Weber, A. Z. New Insights into Perfluorinated Sulfonic-Acid Ionomers. *Chem Rev* **117**, 987-1104 (2017).

80. Paul, D. K., Karan, K., Docoslis, A., Giorgi, J. B. & Pearce, J. Characteristics of Self-Assembled Ultrathin Nafion Films. *Macromolecules* **46**, 3461-3475 (2013).

81. Zhao, J. *et al*. A Wearable Nutrition Tracker. *Adv Mater* **33**, 2006444 (2021).

82. Ma, C. *et al*. Morphology and properties of Nafion membranes prepared by solution casting. *Polymer* **50**, 1764-1777 (2009).

83. Wang, Y. A Membrane Biosensor for the Detection of Lactate in Body Fluids. (University of Waterloo, Waterloo, 2018).

84. Gerlache, M., Senturk, Z., Quarin, G. & Kauffmann, J. Electrochemical behavior of H2O2 on gold. *Electroanalysis* **9**, 1088-1092 (1997).

85. Yorita, K. *et al*. Conversion of L-Lactate Oxidase to a Long Chain α-Hydroxyacid Oxidase by Site-directed Mutagenesis of Alanine 95 to Glycine *. *J Bio Chem* **271**, 28300-28305 (1996).

86. Nakamura, S., Hayashi, S. & Koga, K. Effect of periodate oxidation on the structure and properties of glucose oxidase. *Biochimica et Biophysica Acta Enzymology* **445**, 294-308 (1976).

87. Moussa, S., Chhin, D., Pollegioni, L. & Mauzeroll, J. Quantitative measurements of free and immobilized RgDAAO Michaelis-Menten constant using an electrochemical assay reveal the impact of covalent cross-linking on substrate specificity. *Anal Bioanal Chem* **413**, 6793-6802 (2021).

88. Lyons, M. E. G. Transport and kinetics in electrocatalytic thin film biosensors: bounded diffusion with non-Michaelis-Menten reaction kinetics. *J Solid State Electrochem* **24**, 2751-2761 (2020).

89. Abrar, M. A., Dong, Y., Lee, P. K. & Kim, W. S. Bendable Electro-chemical Lactate Sensor Printed with Silver Nano-particles. *Sci Rep* **6**, 1-9 (2016).

90. Lamas-Ardisana, P. J. *et al*. Disposable amperometric biosensor based on lactate oxidase immobilised on platinum nanoparticle-decorated carbon nanofiber and poly(diallyldimethylammonium chloride) films. *Biosens Bioelectron* **56**, 345-351 (2014).

91. Hashemzadeh, S., Omidi, Y. & Rafii-Tabar, H. Amperometric lactate nanobiosensor based on reduced graphene oxide, carbon nanotube and gold nanoparticle nanocomposite. *Microchim Acta* **186**, 680 (2019).

92. Payne, M. E., Zamarayeva, A., Pister, V. I., Yamamoto, N. A. D. & Arias, A. C. Printed, Flexible Lactate Sensors: Design Considerations Before Performing On-Body Measurements. *Sci Rep* **9**, 1-10 (2019).

93. Hernández-Ibáñez, N. *et al*. Electrochemical lactate biosensor based upon chitosan/carbon nanotubes modified screen-printed graphite electrodes for the determination of lactate in embryonic cell cultures. *Biosens Bioelectron* **77**, 1168-1174 (2016).

94. Zeng, Y. *et al*. Functionalization of multi-walled carbon nanotubes with poly(amidoamine) dendrimer for mediator-free glucose biosensor. *Electrochem Commun* **9**, 185-190 (2007).

95. Rernglit, W., Teanphonkrang, S., Suginta, W. & Schulte, A. Amperometric enzymatic sensing of glucose using porous carbon nanotube films soaked with glucose oxidase. *Microchim Acta* **186**, 616 (2019).

96. Guadarrama-Fernández, L. *et al*. Characterization of Functionalized Multiwalled Carbon Nanotubes for Use in an Enzymatic Sensor. *Microsc Microanal* **20**, 1479-1485 (2014).

97. Hua, M., Lin, Y., Tsai, R., Chen, H. & Liu, Y. A hydrogen peroxide sensor based on a horseradish peroxidase/polyaniline/carboxy-functionalized multiwalled carbon nanotube modified gold electrode. *Electrochim Acta* **56**, 9488-9495 (2011).

98. Liu, Y., Tang, J., Chen, X. & Xin, J. H. Decoration of carbon nanotubes with chitosan. *Carbon* **43**, 3178-3180 (2005).

99. Lee, D. W., Lim, C., Israelachvili, J. N. & Hwang, D. S. Strong Adhesion and Cohesion of Chitosan in Aqueous Solutions. *Langmuir* **29**, 14222-14229 (2013).

100. Shieh, Y., Wu, H., Twu, Y. & Chung, Y. An investigation on dispersion of carbon nanotubes in chitosan aqueous solutions. *Colloid Polym Sci* **288**, 377-385 (2010).

101. Cai, C. & Chen, J. Direct electron transfer of glucose oxidase promoted by carbon nanotubes. *Anal Biochem* **332**, 75-83 (2004).

102. Choi, Y. *et al*. The electrochemical glucose sensing based on the chitosan-carbon nanotube hybrid. *Biochem Eng J* **144**, 227-234 (2019).

103. Zhang, M., Smith, A. & Gorski, W. Carbon Nanotube−Chitosan System for Electrochemical Sensing Based on Dehydrogenase Enzymes. *Anal Chem* **76**, 5045-5050 (2004).

104. Clasen, C., Wilhelms, T. & Kulicke, W. -. Formation and Characterization of Chitosan Membranes. *Biomacromolecules* **7**, 3210-3222 (2006).

105. Hirotaka, N. *et al*. Diameter and rigidity of multiwalled carbon nanotubes are critical factors in mesothelial injury and carcinogenesis. *Proc Natl Acad Sci USA* **108**, E1330-E1338 (2011).

106. Shadmehr, S., Coleman, M., Liu, B., Liu, J. & Tang, X. (Shirley). Reversible gating of ion transport through DNA-functionalized carbon nanotube membranes. *RSC Adv* **7**, 611-616 (2017).

107. Liu, K. *et al*. Controlled Growth of Super-Aligned Carbon Nanotube Arrays for Spinning Continuous Unidirectional Sheets with Tunable Physical Properties. *Nano Lett* **8**, 700-705 (2008).

108. Luo, Q. *et al*. Carbon Nanotube/Chitosan-Based Elastic Carbon Aerogel for Pressure Sensing. *Ind Eng Chem Res* **58**, 17768-17775 (2019).

109. Alshahrani, A. A., Al-Zoubi, H., Nghiem, L. D. & in het Panhuis, M. Synthesis and characterisation of MWNT/chitosan and MWNT/chitosan-crosslinked buckypaper membranes for desalination. *Desalination* **418**, 60-70 (2017).

110. Mane, S., Narmawala, R. & Chatterjee, S. Selective recognition of atropine in biological fluids and leaves of Datura stramonium employing a carbon nanotube–chitosan film based biosensor. *New J Chem* **42**, 10852-10860 (2018).

111. Li, C. G., Dangol, M., Lee, C. Y., Jang, M. & Jung, H. A self-powered one-touch blood extraction system: a novel polymer-capped hollow microneedle integrated with a pre-vacuum actuator. *Lab Chip* **15**, 382-390 (2014).

112. Wolf, M. P., Salieb-Beugelaar, G. B. & Hunziker, P. PDMS with designer functionalities—Properties, modifications strategies, and applications. *Prog Poly Sci* **83**, 97-134 (2018).

113. Wang, Z., Volinsky, A. A. & Gallant, N. D. Crosslinking effect on polydimethylsiloxane elastic modulus measured by custom-built compression instrument. *J Appl Poly Sci* **131** (2014).